CHALMERS
UNIVERSITY OF TECHNOLOGY

Large Eddy Simulation of transitional flow over a flat plate

Master's thesis in Applied Mechanics

ABHISHEK SARAF

Large Eddy Simulation of transitional flow over a flat plate

ABHISHEK SARAF

Large Eddy Simulation of transitional flow over a flat plate
Master's Thesis in Fluid Dynamics

iv

Abstract

The transition of the laminar boundary layer to turbulence in the free stream is of major importance in turbomachinery flows. Transition in the boundary layer has a big impact on flow parameters such as skin friction coefficient and shape factor thereby affecting the design and development process. It is known that the boundary-layer transition is affected by properties of the free-stream turbulence such as its anisotropy, length scale and its intensity. In the present thesis a Large-Eddy Simulation (LES) has been performed of a zero pressure gradient flat-plate boundary layer undergoing transition to turbulence under free-stream turbulence at a level of 6%. In the current work the bypass transition is defined as a superposition of the Blasius layer with freestream continuous isotropic turbulence at an initial intensity level of 6%. An effort is made to capture the length and position of boundary layer transition over the flat plate and a subsequent comparison of the skin friction coefficient and shape factor were made with the experimental data. A finite volume method based in-house solver in Fortran, namely CALC-LES, is used for performing the simulations. The solver of CALC-LES is based on a geometric multigrid algorithm to solve the pressure (poisson) equation. Three different subgrid scale (SGS) models are used for performing comparative studies – the Smargorinsky-Lilly model, the Wall-adapting local eddy-viscosity (WALE) model and the Scale-similarity model. The experimental data for the skin friction coefficient and shape factor were used as a basis to ascertain whether the present simulation manages to capture transition. The present simulations fail to capture the transition appropriately in the boundary layer over the flat plate. The dimensionless coefficients, namely the skin friction coefficient and the shape factor are not in the exact accordance with the experimental data. The mesh independence study showed that the stream-wise resolution hardly played any role in the transition. The study of the resolved Reynolds stress components in the boundary layer revealed that the stream-wise stress component decreased in magnitude significantly, but it doesn't get distributed into the other components. As a result transition is not observed. Upon further inspection of the turbulent kinetic energy peak showed that probably the stream-wise streaks grow, but either they were not big enough to trigger transition or there was no continuous forcing provided by the free-stream turbulence to trigger transition. It is not known what aspect of the current LES simulations are at fault but in the light of the general level of agreement obtained, we conclude that,the the simulation qualitatively mimics the real boundary layer even though precise quantitative agreement is not found for all variables.

Keywords: CFD, LES, boundary layer transition, bypass, FST, flat plate .

Acknowledgements

I would like start by firstly expressing my gratitude towards my thesis supervisor Prof. Lars Davidson, for being patient and encouraging me to experiment with different methods during my thesis. I would also like to acknowledge my colleagues, Srikanth and Amith, for their support during my masters studies. I am specially thankful to Srikanth for providing his valuable critique on my thesis report.

Finally, I would like to express my profound gratitude towards my parents, sister and brother-in-law for their constant support and advice.

Abhishek Saraf, Göteborg, 2016/09/05

Nomenclature

Abbreviations

DNS   Direct Numerical Solution
FST   Free-stream Turbulence
LES   Large Eddy Simulations
LKE   Laminar Kinetic Energy
MG   Multi-grid
NS   Navier-Stokes
PPE   Pressure Poisson Equation
RANS   Reynolds-averaged Navier-Stokes equations
rms   Root mean square
SGS   Sub-grid scale
TKE   Turbulent Kinetic Energy
WALE   Wall adapting local eddy-viscosity model

Greek Symbols

$\bar{\Delta}$ Grid filter-width
δ_{ij} Kronecker-delta
κ von Kármán constant
ν Kinematic viscosity
ν_r Residual/SGS eddy-viscosity
ρ Density
τ_r Residual/SGS stress tensor

Roman Symbols

C_s Smagorinsky coefficient
C_w WALE coefficient
I Turbulent Intensity
l_{smg} Smagorinsky lengthscale
L_t Integral length scale
l_{wale} WALE lengthscale
Pr Molecular Prandtl Number
S_{ij} Strain-rate tensor, $S_{ij} = \frac{1}{2}\left(\frac{\partial v_i}{\partial x_j} + \frac{\partial v_j}{\partial x_i}\right)$
U_o Inlet Velocity
v Velocity
V   Volume

Subscripts

$(.)_i$ Einstein-notation

Superscripts

$\overline{(.)}$ Spatial Grid-filtering

Contents

1
Introduction

The present study is concerned with the flow over a flat plate a flat plate subject to free-stream turbulence. The bypass transition studied is that specified in the ERCOFTAC test case T3 [31], in which a free-stream turbulence level of 6% is superimposed on a parallel flow of $U_o = 9.6m/s$. The behaviour and properties of fluid flows are important in many different technical applications of today's industrial world. One of the most relevant characteristics of a fluid is the flow state in which it is moving i.e. laminar, turbulent or the transitional state in between. The laminar flow is a well predictable, structured and layered flow, which usually exercises significantly less frictional resistance to solid bodies and much lower mixing rates than the chaotic, swirly and fluctuating state of fluid in turbulent motion. Understanding and predicting both turbulent and laminar flow is crucial in a variety of technical applications, e.g. flows in boundary layers on aircraft wings, around cars, intermittent flows around turbine blades, and flows in chemical reactors or combustion engines. The evolution of an initially laminar flow into a fully developed turbulent flow is called laminar-turbulent transition. There are several approaches of promoting the downstream flow to bypass transition to turbulence such as blowing and suction at the wall, passing wakes, trip wire, roughness element, oblique waves or body forces.

Transition in the boundary layer is of significant importance to practical applications such as aerodynamics of wings, turbomachinery etc. as the factors such as heat transfer, skin friction drag on the surface affects the overall performance. In order to understand or simulate complex geometries using LES, it is advisable to first understand how to obtain transition in the boundary layer in the case of a simple geometry such as a flat plate. If the transition can be obtained for the simple geometry then a set of inlet and boundary conditions as well as transition mechanisms can be determined and then applied to complex geometries. Numerous studies on this mechanism have been carried out till date, both experimental and numerical. Computationally, it is very difficult to capture the transition at high free-stream turbulence (FST) levels as it is governed by non-linear interactions between boundary layer and FST disturbances and termed as bypass transition. In the absence of a specific mathematical model capable of capturing the non-linear growth mechanisms leading to transition and is difficult to contrive. One method to develop understanding in this domain, the governing factors need to be evaluated individually and understand their individual effects. The interaction of free-stream turbulence with the other instability inducing factors in the boundary layer contributes to the growth of the non-linear modes predominantly and transition is

observed in the presence of such high levels of free-stream turbulence, for flows with Reynolds number (Re) even lower than the critical Re computed using the classical linear stability theory. Many of the previous efforts were based on either direct numerical simulations (DNS) or Large eddy simulations (LES), non-modal linear stability analysis, linear and non-linear optimization techniques for largest energy growth of instability modes etc..

1.1 Previous Work

The experiments for the ERCOFTAC T3B case [31] were conducted by Roach and Brieley [28]. One of the earliest works on boundary layer transition using LES includes the simulations on flat plate boundary layer by Voke and Yang [34]. They observed transition on a very coarse mesh with resolution based on wall units as, $\Delta x^+ \simeq 80$, $\Delta z^+ \simeq 14$ and $\Delta y^+ \simeq 1$ at the wall to 80 beyond the boundary layer. The wall units were computed based on friction velocity just after transition.

1.2 Why LES?

The RANS based modelling approaches are usually employed to simulate transitional flows, due to their computational cost effectiveness. One method is to employ a simple 'point transition' approach whereby a transition is forced between laminar and turbulent computations at a point determined either by empirical correlations, algebraic models, DNS or experimental data. Another method is to employ a three-equation model based on the low-Reynolds $k - \omega$ model with an equation for the so called laminar kinetic energy k_L expressing the energy of stream-wise fluctuations in pre-transitional region. A good overview of the early developments on these methods is given by Savill [30]. A shortcoming of using the RANS methods is that all spectral effects are lost in the time averaging process. However, bypass transition is supposed to be very sensitive to the spectral nature of the imposed FST. Therefore, the RANS methods is not likely to reliably capture all factors that affect transition for various combinations of FST intensity, Reynolds number and pressure gradients, and are found to be very sensitive to initial conditions and boundary conditions. In the LES approach, the smallest scales of motion are modelled, preserving the spectral nature of the larger energy containing eddies. In this respect, it is better than the RANS approach on the grounds of predicting transition more accurately.

1.3 Aim and Scope

The main aim of the present study is to capture transition based on FST disturbances using artificial fluctuations. The onset and length of transition is not the immediate concern in the present study. The main objective is to reproduce the LES performed by Voke and Yang [34] to study the boundary layer transition over a flat plate subject to FST and managed to capture transition using a coarse mesh. The report can be divided broadly into four parts:

- Explain the mechanisms and stages involved in bypass transition. - Chapter 2.
- Brief description of LES, the governing equations, SGS models to be used, and the pressure poisson equation. - Chapter 3.
- Experimental setup flow conditions, computational domain setup, mesh properties, case setup, and boundary conditions. - Chapter 4.
- Results, discussion, conclusion and future work. – Chapter 5 and 6.

2

Boundary Layer Transition Theory

In the case of wall-bounded flows, the laminar-turbulent transition is very sensitive to perturbations/external disturbances in initial conditions, boundary conditions and surface (roughness) properties. These perturbations initiate the transition of an initially laminar flow to a turbulent flow. The ability to control the transition greatly increases engineering efficiency and performance such as aerodynamics and turbomachinery.

The present study is focused around the investigation of laminar-turbulent transition in the boundary layer of the flow over a flat plate in a zero pressure gradient condition. In the case of the flat plate, at the leading edge, the fluid particles close to the wall are slowed down due to viscosity, the closest one coming to rest instantaneously (no-slip condition). Due to this there is a sudden increase in static pressure at the edge. As the fluid moves further downstream, additional layers parallel to the surface start getting affected due to viscosity. At a certain distance from the wall in normal direction the velocity reaches the free-stream value. This distance keeps increasing in the stream wise direction, as more and more layers of fluid start getting affected by the wall (the boundary layer increases downstream). The type of flow in the boundary layer near the leading edge is essentially laminar. After a certain distance downstream however, the flow in the boundary layer starts getting chaotic, marking the onset of transition. Further downstream, the flow gets completely turbulent. This is characterized by an increase in wall shear stress. Due to the incomplete understanding of the triggering mechanisms, a single approach to capture transition cannot be ascertained.

In the following section, a literature survey is conducted to better understand the different mechanisms and paths leading to transition.

2.1   Paths of transition to turbulence

The perturbations in the initial conditions, boundary conditions or surface conditions such as roughness may interact with the boundary layer thereby creating instabilities. The development of such instabilities in a laminar flow can possibly lead to transition to turbulent flow. The interaction between external disturbances and the boundary layer instabilities is referred to as receptivity. Saric et al. [29] based on some earlier studies, illustrated a simplified scenario for turbulence transition in external flows. Figure 2.1 depicts the same.
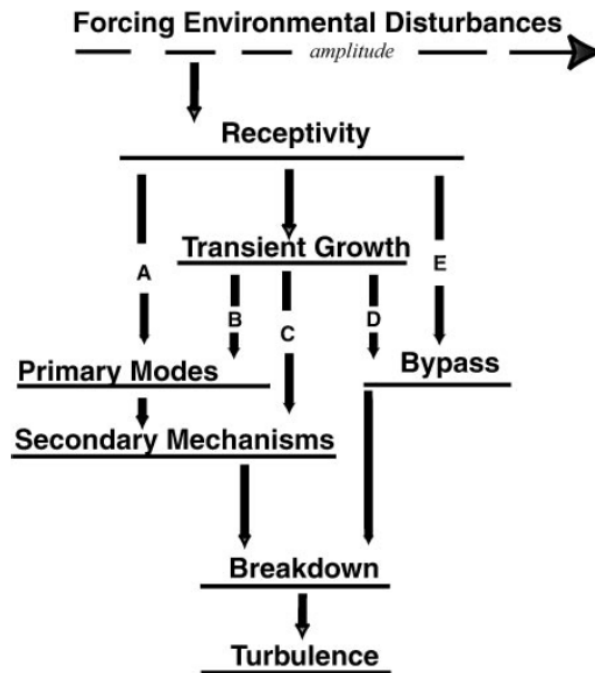
Figure 2.1: The paths from receptivity to transition [29]

According to the figure 2.1, the initial external disturbance amplitude increases from left to right schematically. Starting with receptivity, a number of different instabilities can occur independently or together depending on the Reynolds number, wall curvature, surface roughness or initial conditions and one of the five different paths shown is followed. The path A is followed when a very low free stream turbulence (FST) level at the inlet, generally equal to or below 1% of the mean flow. The first stage in such type of transition is the development of two-dimensional Tollmien-Schlichting(TS) waves, which can be predicted by the modal/eigenvalue analysis of the linearized Navier-Stokes(NS) equations. These instabilities grow exponentially and goes on to evolve on large viscous time scales. As the amplitude grows, the interactions take place on convective time scales and are three-dimensional in nature. Such interactions are explained using the secondary instability theory. This is followed by the appearance of small-scale motions and the final stages of transition. Such a kind of transition is called natural transition. The theoretical and experimental work based on this type of transition is studied by Kachanov [16].

The transition achieved via the paths B, C and D are based on the evolution of the initial boundary layer instability and reffered to as the transient growth mechanisms. A non-modal analysis of the linearized NS equations, is used to study this type of transition mechanism. Schmidt [32] has compiled a review of non-modal stability analysis.

In the case of the free stream turbulence (FST) level greater than 1%, the transition will enters into the non-linear interaction stage directly, and the linear instability stage marked by the formation and growth of TS waves is bypassed. It is

referred to as bypass transition(path D and E). It is characterized by the appearance of stream-wise elongated streaky structures(referred to as Klebanoff modes) of alternating high and low stream-wise velocity in the laminar boundary layer, which grow in magnitude as they move downstream and finally lead to complete breakdown resulting in turbulence [1]. The majority of the mechanisms of bypass transition follow the path D.

2.2 Bypass-transition mechanisms

Klebanoff [18] first observed the occurrence of stream-wise elongated structures with alternating positive and negative stream-wise disturbance velocities in laminar boundary layers subjected to FST. As per his study, the FST amplitude and boundary layer thickness was found proportional to the amplitude of the peak response of such structures. The Klebanoff modes were also observed in the experimental studies conducted by Kendall [17] and observed similar results for flow subject to FST. The Klebanoff modes are usually depicted in terms of rms profiles of stream-wise velocity in the boundary layer. Matsubara & Alfredsson [21] reviewed several experiments performed at the Royal Institute of Technology (KTH). Their experiments found that the span-wise spacing of streaks, usually of opposite sign of the u'-velocity perturbation increases with the FST level, and also slightly increases with the stream-wise distance. Towards the end of the transition zone, it was approximately equal to the boundary-layer thickness.

Bypass transition is characterized with the occurrence of stream-wise streaks in the boundary layer. The stream-wise velocity grows linearly in time in the presence of a disturbance with no stream-wise variation. This is ascribed to the lift-up and vortex-stretching mechanism or more accurately to the vortex tilting mechanism. The normal vorticity increases in time due to the tilting of cross-stream (span-wise) vorticity by the perturbation strain rate in span-wise direction (this disturbance can be viewed as a stream-wise vortex). Since the disturbance is elongated in the stream-wise direction due to the mean shear, the final effect can be seen as streaks with high and low stream-wise velocity fluctuations. A good description can be found in the introduction of the article by Butler and Farrell [6].It is believed that in the presence of viscosity though, such inviscid amplifications eventually decay after a short time or short stream-wise distance. This phenomenon is termed as transient growth. It is then possible for a sufficiently amplified disturbance, before decay sets in, to trigger non-linear interactions and cause breakdown to turbulence.

The amplification of transient energy is not due to the behaviour of a single eigen-mode of the linearized disturbance equation as found in exponentially growing TS waves. The redistribution of span-wise vorticity into stream-wise-periodic lumps near the critical layer, the growth of 3D modes arises from the combined effects of vortex tilting and stretching and called non-modal growth as well. Grossmann[12] details these mechanisms on shear flow turbulence.

The initial disturbance able to induce maximum transient growth at a given time

is referred to as optimal. The transient growth mechanism is linear in nature and has been studied extensively using optimization techniques. Butler and Farrell [6] used variational methods and deduced the optimal perturbation responsible for the maximum transient growth in a boundary layer for Couette and Poiseuille flows. It was observed that perturbations in the form of stream-wise/longitudinal vortices are responsible for inducing the greatest energy growth in the laminar boundary layer in the form of powerful stream-wise streaks, that can be related to the Klebanoff modes found in the pre-transitional boundary layer in the bypass transition case. In the studies conducted by Andersson et al. [2] and Luchini [19], a spatial instability problem was formulated in contrast to the temporal instability problem by Butler and Farrell [6]. It is observed that the optimal perturbation consisted of a pair of counter rotating stream-wise vortices outside the boundary layer. In addition, the critical streak amplitudes for the sinuous and varicose instabilities were observed to be 26% and 37%, respectively. Luchini [19] also found that the shape of the streaks in the pre-transitional boundary layer tends to be attracted towards the shape of the optimal perturbation (Klebanoff modes), even for non-optimal initial perturbations. The shape was found to be insensitive to a wide range of wavenumbers, frequencies and shape of the initial perturbation.

A comprehensive experimental study of the disturbance growth inside the boundary layer was conducted by Matsubara et al. [21]. The results of the experiments were in accordance with the linear non-modal growth mechanism of the boundary layer streaks. The Direct Numerical Simulation (DNS) of flow over a flat plate was conducted by Jacobs and Durbin [14], by considering the inflow FST as a sum of span-wise and temporal fourier modes, multiplied by wall-normal Orr-Sommerfeld modes. Only the continuous spectrum of the latter was considered due to their inherent property of being sinusoidal in the free-stream and approaching to zero near the wall. The concept of shear sheltering was introduced by Jacobs and Durbin [13] that the disturbances convected with free-stream velocity did not couple to the fluid in the shear layer near the wall. The penetration depth of such disturbances was found to be inversely proportional to their frequency and the Reynolds number based on the distance from the leading edge, thus establishing that streaks are an implicit property of the boundary layer. Brandt et al. [5] in their DNS study of a flat plate boundary layer, also used the continuous spectrum of the Orr-Sommerfeld equation to generate inflow boundary condition similar to Jacobs and Durbin and included the Squire modes for the wall-normal vorticity. They observed that the onset of transition moves upstream with an increase in the FST length scale. However, like in the Jacobs and Durbin study [14], the span-wise scale of the streaks inside the shear layer was found to be highly insensitive towards the details of inlet turbulence (FST). With fine, turbulent-like resolution in the entire boundary layer, they obtained very good agreement with the T3A experiment of Roach & Brierley [28] at 3% FST intensity. Klebanoff modes were found to be a prominent feature of their simulations, and were generated non-linearly by the penetration of the FST into the boundary layer Jonas et al. [15] performed as experiments on flat plate boundary layer, and also concluded that the onset of transition moved upstream with increasing FST length scale. Brandt et al. [5] also concluded that for receptivity, linear

mechanism is most relevant if the FST contains low-frequency disturbances, whereas, non-linear mechanism takes over if the FST contains high-frequency disturbances. Berlin and Henningson [4] had proposed a non-linear receptivity mechanism based on their spectral DNS study of Blasius flow with both temporal and spatial formulations and observed that the non-linear mechanism is responsible for generating wall-normal perturbations associated with stream-wise vortices inside the boundary layer, which on interacting with the boundary layer shear produce the stream-wise streaks. At levels of low FST intensity levels linear mechanism dominate, whereas non-linear mechanism plays important role at higher FST levels. At moderate disturbance levels, both mechanisms produce streaks of similar strength. The growth of streaks is supposed to be based on linear transient mechanism i.e. it is only characterized by the appearance of streaks, which could be linear or non-linear. The importance of wall-normal velocity in the free-stream for inducing transition was also emphasized by Voke and Yang [34] in their LES study of flow over a flat plate. The factors affecting penetration depth of free stream turbulence was studied by Zaki et al. [38]. In their study, the Orr-Sommerfeld/Squire eigenvalue problem were analyzed and concluded that the penetration depth inside a boundary layer shear depended on the following paramets: Inversely proportional to the frequency of disturbance, Reynolds number, the local mean shear at the wall and increases with increasing wall-normal wavenumber. Additionally, an increase in the wall-normal wavenumber, leads to an increase in the decay rate but it does persist far downstream of the leading edge. A coupling coefficient was defined that depicted the local interaction of continuous Orr-Sommerfeld modes and the boundary layer. It represented the penetration ability of the modes in the boundary layer and also its ability to generate streaks. Not all penetrating modes generated streaks; the ones with high decay rate failed to do so, e.g. disturbances with high wall-normal wavenumber. Disturbances with low frequencies and small wall-normal wavenumbers had higher coupling coefficients.

The effect of Pressure gradient has a significant effect on the receptivity process. The study conducted by Zaki et al. [37] resulted in lower shear at the wall in the case of zero pressure gradient in comparison to the adverse pressure gradient case. The onset and location of transition is observed to be is delayed in the case of the adverse pressure gradient case. This is attributed to the fact that streak formation is higher in magnitude for adverse pressure gradient in comparison with the zero pressure gradient cases, hence more sensitive to FST.

Most of the studies on transient growth assumed parallel flow, thereby neglecting the effect of the leading edge(non-parallel flow). The numerical study conducted by Zaki and Durbin [38] consider a leading edge. In their case at the leading edge, as boundary layer thickness $\delta \longrightarrow 0$, all modes act as low frequencies and become penetrating; but since $Re_x \longrightarrow 0$ (Re based on distance from leading edge), they also decay rapidly. They conclude that the coupling leading to boundary layer streaks and transition is local, and occurs downstream of the leading edge. A non-linear method discussed by Berlin and Henningson [4] forced streaks in the boundary layer locally even downstream of the leading edge. Goldstein and Wundrow [20] consider

the leading edge and show that FST containing wake like disturbances, corresponding to wall-normal vortical structures, get stretched and tilted around the leading edge and transform into low frequency modes corresponding to stream-wise aligned vortices. These vortices then penetrate in the boundary layer to produce streaks. It was observed that the leading edge just enhances the growth of Klebanoff modes inside the boundary layer; the mechanism to transition still remains the same. Nagarajan et al. [23] carried out simulations on a flat plate boundary layer with a blunt elliptical leading edge. They observed that a blunter leading edge, gives free stream conditions, exhibits earlier onset and completion of transition. In addition, it was found the same mechanism is in play around the leading edge as observed by Goldstein and Wundrow– stretching and tilting of vortices around the leading edge.

The stream-wise elongated unsteady streaks in the boundary layer are the main driving source of bypass transition. The mechanisms driving the conversion of streaks into turbulent spots and subsequent break-down have been an important aspect of bypass transition studies. Jacobs and Durbin [14] observe that streaks with negative stream-wise fluctuation ($u' < 0$), termed as negative jets, are responsible for the formation of turbulent spots. They are present predominantly in the upper boundary of the shear layer and are continuously in contact with the high frequency free-stream disturbances outside the boundary layer. This implies the development of turbulent spots. The positive jets, predominant close to the surface of the plate, do not undergo instability. Brandt et al. [5] observe that streak break-down and turbulent spot formation is caused by either of two types of instability modes of low-speed streaks (negative jets). The sinuous mode is characterized by streak oscillations in the span-wise direction, was observed more frequently than the varicose mode of instability that is driven by the wall-normal shear. The sinuous mode instability is similar to the backward jet mechanism of Jacobs and Durbin [14]. Zaki et al. [38] in their DNS study used a pair of inflow modes, one with high coupling coefficient (presumably low frequency), and the other a weakly coupled mode (high frequency) and observe that it was sufficient to trigger transition. The low frequency modes generate streaks inside the boundary layer. The fluctuations due to the low frequency modes interact with the fluctuations generated by the high frequency modes, thereby lifting the negative streaks towards the edge of the boundary layer. The latter is unable to penetrate the shear layer and is present in the free-stream. Some of these jets get intensified and burst into turbulent spots. This is also similar to the mechanism observed by Jacobs and Durbin [14].

The DNS study conducted by Nagarajan et al. [23] that identical inflow turbulence field results in different paths to transition depending on the leading edge geometry. There is a shift in the location of onset of transition. Spot precursors responsible for transition were identified to be wavepacket like disturbances originating at the leading edge (blunt). Spot precursor formed at the leading edge inhabited the lower part of the boundary layer. The vortices were aligned normal to the wall and get stretched around the leading edge resulting in localized regions of stream-wise vorticity inside the boundary layer, which grow as they convect downstream. The effect of FST length scales and leading edge on bypass transition were

studied by Ovchinnikov et al. [25]. Their studies concluded that the FST length scales comparable to the boundary layer thickness at the onset of transition, δ_{99}, the transition followed the Klebanoff mode mechanism, whereas for higher FST length scales, comparable to $7\delta_{99}$, the transition followed a different path. They observed that wave packet like disturbances in stream-wise direction act as spot precursors that lead to transition. They are associated with span-wise vortical structures in boundary layer in contrast to stream-wise ones in the simulations of Nagarajan et al. [23]. Initially in spanwise direction, the vortices subsequently reorient themselves partially in stream-wise direction. The result is either a Λ -vortex (two legs) or quasi-streamwise vortex (one-leg). These structures finally develop into spots and subsequently break down to turbulence. They also find that wavepackets appear in wall-normal velocity component as compared to the span-wise component in the simulations of Nagarajan et al. [23] and that they are not confined to the lower part of the boundary layer close to the wall, as was observed by the former. This could be explained as a result of higher Re (based on FST integral length scale) in the study of Ovchinnikov et al.[25] and also the higher FST intensity in their study. The DNS study for a spatially evolving turbulent zero pressure gradient boundary layer over a smooth flat plate, conducted by Wu and Moin [36] and deduced from their flow visualizations that the occurance of boundary layer streaks was merely a kinematic feature, appearing as a result of lift up mechanism. They were not found to be responsible for transition. The non-linear development of obliquely Λ -oriented vortices into hairpin packets was observed to be responsible for the breakdown into transition. However, receptivity of such disturbances inside the boundary layer was not discussed. Cherubini et al. [8] proposed a purely non-linear scenario of (bypass) transition in boundary layer, justifying the preponderance of hairpin structures observed by Wu and Moin [36] in their transitional boundary layer. Using non-linear optimization of the energy growth at short time, they identified the smallest flow structure, called the minimal seed perturbation, responsible for inducing turbulence in the boundary layer. Cherubini et al. [7] concluded that transition in a flat plate boundary layer in the presence of FST, follows a purely non-linear route characterized by the formation of hairpin/Λ vortices, when turbulent intensity and turbulent length scale of the FST are very high (for $I > 4.5\%$ and $l > 20$). In the case of lower intensities and length scales of the FST, the transition was said to follow the traditional streak mechanism (transient growth and secondary instability leading to break-down).

3

Governing Equation and Solution Methods

The governing equations for laminar, transitional and turbulent flows are the Navier-Stokes (NS) equations for the velocity components $u_i (i = 1, 2, 3)$ and the pressure p. The NS equations for an incompressible fluid flow in conservative form and in the absence of body forces is presented as:

$$\frac{\partial v_i}{\partial x_i} = 0 \tag{3.1}$$

$$\frac{\partial v_i}{\partial t} + \frac{\partial v_i v_j}{\partial x_j} = -\frac{1}{\rho}\frac{\partial p}{\partial x_i} + \nu \frac{\partial^2 v_i}{\partial x_j \partial x_j} \tag{3.2}$$

The equations 3.1 and 3.2 represent the continuity and momentum conservation equations respectively. In the absence to achieve an exact analytical solution to these equations, the equations are discretized and solved numerically. There are multiple ways of solving these equations numerically. One way is to solve the time averaged NS equations, where the extra terms appearing out of averaging are modelled: the RANS method. Another way is to resolve the whole range of temporal and spatial scales, without the need for modelling: called the DNS. The latter method requires a very fine grid resolution thus limiting it's practicality due to the high computational cost involved. In the wake of the two methods mentioned above, LES is being used for time accurate prediction of unsteady flows at high Reynolds numbers. In contrast to DNS the Kolmogorov dissipation scale is not resolved in LES, making the computational cost of LES largely independent of the Reynolds number. The level of abstraction is lower than the statistical approaches based on RANS equations. Thus the scope of LES extends to unsteady turbulent flows with a broad range of spatial and temporal scales in which the larger energy containing motions are resolved and the effect of the smaller ones are modelled.

3.1 Large Eddy Simulations

As mentioned earlier, in LES, the larger scales are resolved and smaller ones are modelled. The first step in LES is filtering in which the flow variable (ϕ) is decomposed into a resolved/filtered component ($\bar{\phi}$) and the residual/SGS(sub-grid scale) component (ϕ'). The most commonly used LES approach is the implicitly filtered approach. In implicitly filtered LES, the computational grid and the discretization

operators are considered as the filtering of the governing equations. In the present study, a volume-average box filter is used where the filter-width ($\bar{\Delta}$) is taken as $[\bar{\Delta} = (\Delta V_{IJK})^{\frac{1}{3}}]$. The details about filtering operations can be found in [26]. The equations 3.1 and 3.2, after the filtering operation give rise to a set of equations presented as:

$$\frac{\partial \bar{v}_i}{\partial x_i} = 0 \tag{3.3}$$

$$\frac{\partial \bar{v}_i}{\partial t} + \frac{\partial \bar{v}_i \bar{v}_j}{\partial x_j} = -\frac{1}{\rho}\frac{\partial \bar{p}}{\partial x_i} + \nu \frac{\partial^2 \bar{v}_i}{\partial x_j \partial x_j} - \frac{\partial \tau_{ij}^r}{\partial x_j} \tag{3.4}$$

The effect of the non-resolved small(residual) scales enters in equation 3.4 through the subgrid-scale (SGS) term:

$$\tau_{ij}^r = \overline{v_i v_j} - \bar{v}_i \bar{v}_j \tag{3.5}$$

The τ_{ij}^r is not closed since $\overline{v_i v_j}$ cannot be obtained from the filtered quantities u_i alone. The next step is to obtain closure by modelling τ_{ij}^r by an appropriate SGS model. The energy dissipation due to the SGS stresses τ_{ij}^r is:

$$\varepsilon_{SGS} = \tau_{ij}^r \bar{S}_{ij} \tag{3.6}$$

As per equation 3.6, ε_{SGS} describes the amount of kinetic energy which is dissipated by the SGS model in addition to the (physical) viscous dissipation. It is often argued that a correct prediction of the SGS dissipation is one of the crucial statistical features of a successful LES [22]. In the present study three such models are used for performing LES – the Smagorinsky model [33], the WALE model [24] and the Scale-similarity Model [9].

3.1.1   Smargorinsky model

The most widely-used SGS models are the eddy-viscosity models, given by

$$\tau_{ij}^r - \frac{1}{3}\tau_{kk}^r \delta_{ij} = -2\nu_r \bar{S}_{ij} \tag{3.7}$$

where $\bar{S}_{ij}$ is the filtered strain-rate tensor. The eddy viscosity ν_r is usually modelled according to [33] yielding the Smagorinsky model. This model forms the basis of all other eddy-viscosity models and assumes the Boussinesq hypothesis. The constant of proportionality ν_r is the residual viscosity, also called the SGS viscosity and needs be modelled. Based on the mixing-length hypothesis, the eddy-viscosity is modelled as:

$$\nu_r = l_{smg}^2 |\bar{S}| = l_{smg}^2 \sqrt{2\bar{S}_{ij}\bar{S}_{ij}} \tag{3.8}$$

where, l_{smg} represents the *Smagorinsky lengthscale* and is taken as proportional to the filter-width $\bar{\Delta}$, such that

$$l_{smg} = C_s \bar{\Delta} \tag{3.9}$$

where, C_s is the Smagorinsky coefficient.

In laminar flow regions and in the viscous sublayer of turbulent wall-bounded flows, the SGS model contributions should vanish or at least be very small. Using the classical Smagorinsky as mentioned above, this condition is not necessarily fulfilled since the filtered strain-rate tensor ($\bar{S}_{ij}$) actually peaks at the walls. Nevertheless, for wall-bounded shear flows, transitional or intermittent flows, $ad-hoc$ remedies have to be used to obtain acceptable results such as a low-Reynolds number correction as implemented in [35]. In the present study, the RANS length scale is used as an upper limit to dampen the eddy-viscosity ν_r.

$$\bar{\Delta} = min\left\{(\Delta V_{IJK})^{\frac{1}{3}}, \kappa n\right\} \tag{3.10}$$

where, n is the distance to the nearest wall.

3.1.2 WALE (Wall adapting local eddy-viscosity) model

The WALE model [24] proposed to model the subgrid/residucal viscosity is based on the square of the velocity gradient tensor ($\bar{g}_{ij}$) accounts for the effects of both the strain and the rotation rate of the smallest resolved turbulent fluctuations. The eddy-viscosity can be written in a generic form as:

$$\nu_r = l_{wale}^2 \mathcal{D}_m(\overline{u_i}) \tag{3.11}$$

where, l_{wale} represents the $WALE\ lengthscale$ and is taken as proportional to the filter-width $\bar{\Delta}$, such that

$$l_{wale} = C_w \bar{\Delta} \tag{3.12}$$

where, C_w is the WALE coefficient and the filter-width ($\bar{\Delta}$) is taken the same as mentioned in equation 3.10.

In LES, the eddy-viscosity must not change when the frame of reference is changed, thus the differential operator ($\mathcal{D}_m(\overline{u_i})$) as mentioned in equation 3.11 must be based on the invariants of a tensor which should be representative of the turbulent activity. The differential operator for the WALE model is approximated as:

$$\mathcal{D}_m(\overline{u_i}) = \frac{(\mathcal{S}_{ij}^d \mathcal{S}_{ij}^d)^{\frac{3}{2}}}{(\bar{S}_{ij}\bar{S}_{ij})^{\frac{5}{2}} + (\mathcal{S}_{ij}^d \mathcal{S}_{ij}^d)^{\frac{5}{4}}} \tag{3.13}$$

where,

$$\mathcal{S}_{ij}^d = \frac{1}{2}(\bar{g}_{ij}^2 + \bar{g}_{ji}^2) - \frac{1}{3}\delta_{ij}\bar{g}_{kk}^2 \tag{3.14}$$

By construction, the trace of ($\mathcal{S}_{ij}^d$) is zero and its second invariant remains finite and proportional ($\mathcal{S}_{ij}^d \mathcal{S}_{ij}^d$). Therefore, a LES model based on ($\mathcal{S}_{ij}^d \mathcal{S}_{ij}^d$) will detect turbulence structures with either strain rate, rotation rate or both of the small turbulent structures. The resulting WALE reproduces the proper scaling at the wall ($\nu_r = \mathcal{O}(y^3)$). It is also well-suited for LES as no explicit filtering is needed and only local information is required to build the eddy-viscosity. Thus all the turbulence

structures relevant for the kinetic energy dissipation are detected by the model, the eddy-viscosity goes naturally to zero in the vicinity of a wall so that neither dynamic adjustment nor damping function are needed to compute wall bounded flows, the model produces zero eddy viscosity in case of a pure shear. Thus it is able to reproduce the laminar to turbulent transition process through the growth of linear unstable modes.

3.1.3 Scale-similarity model

The main idea behind the use of scale similarity subgrid models is to use the small scales of LES itslef. The scale-similarity subgrid models consider the largest unresolved scales are similar to the smallest resolved scales. This is the main idea behind the scale similarity model by Bardina et al. [3]. Scale similarity models involves the interactions between the largest subgrid scales and smallest resolved scales, hence there is a need to define these scales. In the present study, a volume-average box filter is used where the filter-width ($\bar{\Delta}$) is taken as $[\bar{\Delta} = (\Delta V_{IJK})^{\frac{1}{3}}]$.The velocity fields are then defined as follows:

$$u_i^{unres} = u_i - \bar{v}_i \tag{3.15}$$

$$\vec{u_i} = \bar{u}_i - \bar{\bar{v}}_i \tag{3.16}$$

$$u_i'' = \bar{u}_i - \bar{\bar{v}}_i \tag{3.17}$$

Equation 3.15 represents the unresolved scales ($\leq \bar{\Delta}$). Equation 3.16 represents the largest subgrid scale part defined by filtering. Lastly, equation 3.17 represents the smallest resolved scales($>\bar{\Delta}$), defined by a second filter on the resolved field. The last two expressions as mentioned in equations 3.16 and 3.17 are identical, so it is assumes that these scales have similar structure, near the grid cutoff. In other words, the SGS stresses for the full velocity field are the same as the ones corresponding to the resolved field $\bar{u}_i$.

$$\tau_{ij}^r = \overline{\bar{v}_i \bar{v}_j} - \bar{\bar{v}}_i \bar{\bar{v}}_j \tag{3.18}$$

In the present study, the backscatter (transfer of energy from small resolved scales to large resolved scales) from a scale similarity model as described by Davidson [9], will be used with an aim to trigger transition in the boundary layer. The equation for the resolved, turbulent kinetic energy, $K = \langle u_i' u_i' \rangle/2$ is given as:

$$\frac{DK}{Dt} + \langle u_j' u_i' \rangle \frac{\partial \langle \bar{u}_i \rangle}{\partial x_j} + \frac{\partial \langle p' u_i' \rangle}{\partial x_i} + \frac{1}{2} \frac{\partial \langle u_j' u_i' u_i' \rangle}{\partial x_j} = \frac{\partial^2 K}{\partial x_j \partial x_j} - \nu \left\langle \frac{\partial u_i'}{\partial x_j} \frac{\partial u_i'}{\partial x_j} \right\rangle - \left\langle \frac{\tau_{ij}^r}{\partial x_j} u_i' \right\rangle \tag{3.19}$$

The last term in the equation 3.19 describes ε_{SGS}, is a source term arising from the SGS stress tensor, which can be positive or negative. When it is positive, forward scattering takes place and when it is negative, back scattering occurs. The back scattering is achieved by defining a sign function as follows:

$$M_{ij} = -\left(-\frac{\partial \tau_{ij}^r}{\partial x_j} \frac{\partial^2 u_i'}{\partial x_j \partial x_j}\right) = -\left(-\frac{\partial \tau_{ij}^r}{\partial x_j} \frac{\partial^2 \bar{u}_i}{\partial x_j \partial x_j}\right) \tag{3.20}$$

where, the sign function M_{ij} is taken as negative. In addition, the sign of the fluctuating velocity (u_i') is not known initially but second derivative of the resolved velocity fluctuations (u_i') is the same as the resolved velocity $(\bar{u}_i)$. Hence the second derivative of the resolved velocity is taken in equation 3.20. Using the sign function, only the dissipative part of the SGS term, $(-\frac{\partial \tau_{ij}^r}{\partial x_j})$, was included in the momentum equations. The subgrid stress term can also be used as a forcing term. Each component of the divergence of SGS stress tensor in equation 3.4 is then multiplied by:

$$\tilde{M}_{ij} = max(M_{ij}, 0) \tag{3.21}$$

which results in,

$$\frac{\partial \tau_{ij}^B}{\partial x_j} = \tilde{M}_{ij} \frac{\partial \tau_{ij}^r}{\partial x_j} \tag{3.22}$$

As per the equations 3.20, 3.21 and 3.22, the subgrid tensor term is included whenever the sign of $(-\frac{\partial \tau_{ij}^r}{\partial x_j})$ is opposite to that of the viscous diffusion. This means that the SGS term, $(-\frac{\partial \tau_{ij}^B}{\partial x_j})$, in the momentum equations acts as a counter-gradient diffusion term. In this way the backscatter can be used as forcing to trigger transition. In the present study, the scale similarity is applied to the boundary layer along the entire stream-wise direction.

3.2 Solving for the pressure field: PPE

In case of an incompressible flow, there is no explicit equation for solving pressure. Pressure is involved in the momentum equations 3.2 and in general, it is solved indirectly by making use of the continuity equation 3.1. In the present case, pressure is computed directly by solving a Pressure Poisson equation (PPE). The consistent PPE is derived by taking divergence over the momentum equation 3.2:

$$\frac{1}{\rho} \frac{\partial^2 \bar{p}}{\partial x_i \partial x_i} = -\frac{\partial^2 \bar{v}_i}{\partial x_i \partial t} - \frac{\partial^2 \bar{v}_i \bar{v}_j}{\partial x_i \partial x_j} + \nu \frac{\partial^3 \bar{v}_i}{\partial x_i \partial x_j \partial x_j} - \frac{\partial^2 \tau_{ij}^r}{\partial x_i \partial x_j} \tag{3.23}$$

By application of adequate boundary conditions, and imposing the divergence of velocity field to go to zero – the continuity equation – the above equation can be solved. In the present numerical method, an intermediary velocity field from the NS equations devoid of the implicit Pressure gradient term is first solved. A similar PPE as above is formulated by imposing the requirement of continuity on the correct velocity field. The formulation and the whole projection method to solve the system of equations is explained in [11]. The effectiveness of the afore mentioned fractional step projection method mentioned is based on the efficiency of the PPE matrix solver. To solve the PPE, a Geometric Multigrid (GM) algorithm is employed, which is explained in brief in [27].

4

Geometry and Case Set-up

4.1   Overview of experimental flow conditions

The experiment conducted by Roach and Brieley [28] for the ERCOFTAC T3B case [31] is used for comparison with the LES conducted in the present study. The test plate measures $1700mm \times 20mm$ in the $x-direction$ (stream-wise) and $z-direction$ (span-wise) respectively, having leading edge radius of $0.75mm$. The inlet flow conditions for the experiment are en-numerated in Table 4.1. The experimental data at four $x-stations$ (stream-wise), i.e. 25, 45, 95, and 195 mm from the leading edge of the flat plate is used as a basis to evaluate the results of the present LES.

Inlet velocity	U_o	$9.6m/s$
Turbulent intensity	I	6%

Table 4.1: Inlet flow conditions
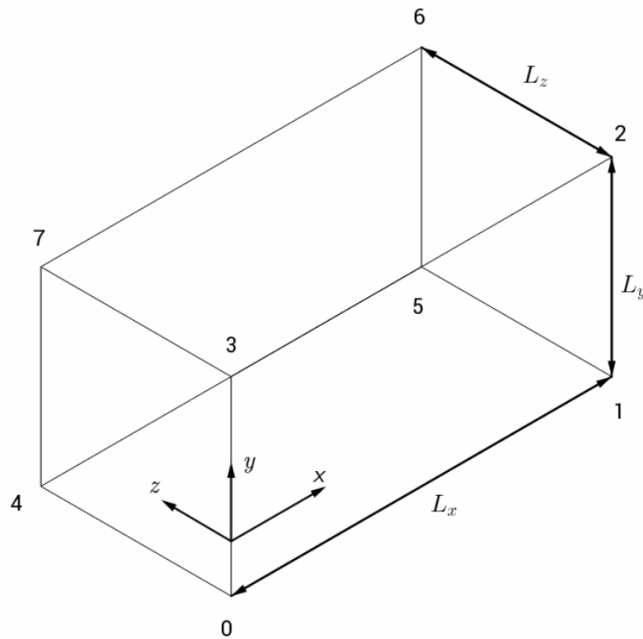
Figure 4.1: Schematic of the computational domain

4.2 Computational domain and case set-up

The geometry for the simulation of transitional flow over a flat plate is given in Figure 4.1. The computational box for the LES starts at $x = 10mm$ downstream of the leading edge, thereby the transition under 6% FST is performed in a domain extending from $Re_x = 6620$ to $Re_x = 200000$. The $stream-wise$, $wall-normal$ and $span-wise$ dimensions of the box are $L_x = 300mm$, $L_y = 30mm$ and $L_z = 20mm$ respectively. The dimensions of the computational box are taken in accordance with the LES performed by Voke and Yang [34].

4.2.1 Mesh and boundary specific restrictions

A Cartesian mesh is generated for the computational domain described in Figure 4.1. In order to conduct a mesh independence study, two sets of meshes are generated namely MESH-I and MESH-II, having an overall resolution of (128×64×48) and (256×64×48) respectively. The wall units are based on the local wall friction velocity as mentioned in the work by Voke and Yang [34]. The details of the mesh for the present study are summarized in Table 4.2.

	MESH-I	MESH-II
N_x	128	256
N_y	64	64
N_z	48	48
Δ_x	2.30 mm	1.17 mm
Δ_z	0.40 mm	0.40 mm
Δ_x^+	78	40
Δ_y^+	1-66	1-66
Δ_z^+	14	14

Table 4.2: Meshing of the simulations - N_x, N_y, N_k denote the number of cells in each direction.

The Geometric Multigrid (GM) method to solve the pressure poisson equation(PPE), as mentioned in section 3.2, restricts the number of cells in each direction. In the present study, the stream-wise grid spacing of MESH-I is twice the one in MESH-II, therefore, the number of cells in the stream-wise direction should be a multiple of 2^n, where n is the desired number of levels.

Face	
(0-3-7-4)	Inlet
(1-2-6-5)	Outlet
(3-2-6-7)	Symmetry
(0-1-5-4)	Wall
(0-1-2-3) and (4-5-6-7)	Periodic

Table 4.3: Boundary specifications

The vertices of the computational box as shown in Figure 4.1 are used to define the specific boundaries. The Table 4.3 represents the vertices of the computational box that enclose faces and mention their corresponding boundary type.

4.2.2 Boundary conditions

Fluid properties		
Density	ρ	1
Prandtl no.	Pr	0.7
Inlet conditions		
Inlet velocity	U_{in}	Blasius profile
Reynolds no.	R_e	6620

Table 4.4: Simulation flow conditions

Inflow	Dirichlet(U_{in})
	Neumann($\frac{\partial p}{\partial n} = 0$)
	Forced inlet fluctuations
Outflow	Convective BC for u,v,w
	Neumann for p
Walls	No-slip(u=v=w=0), Neumann for p

Table 4.5: Boundary conditions: u, v, w and p denote x, y, z components of velocity respectively.

Synthetic fluctuations		
Turbulent intensity	I	6%
Turbulent length scale	L_t	2.4×10^{-3}m
Turbulent time scale	$\mathcal{T}$	2.5×10^{-4}s

Table 4.6: Inlet turbulence: Simulations

INFLOW BOUNDARY : The upstream boundary of the computation domain as shown in Figure 4.1 represents a point 10 mm downstream of the leading edge of the flat plate (Re_x=6620). In order to define the inflow boundary, fixed values of velocity are used (specified in Table 4.4). An appropriate Blasius velocity profile is specified at the inlet boundary. A zero Neumann boundary condition for pressure is specified in order to solve the PPE at both the inlet, outlet and wall. The velocity fluctuation field is based on the turbulence intensity and turbulent length-scales mentioned at the inlet. This will characterize the different scales of motion in the FST, which is crucial in triggering transition.

INLET FLUCTUATIONS: The turbulence conditions at the inflow boundary are prescribed using synthetic isotropic fluctuations. The free-stream disturbances are

generated using the method specified by Davidson in [10], but are limited to the region above y=0.3 mm. The free-stream disturbances at the inflow of the simulations decay rapidly at first, but within a very short distance downstream, attains a more physically realistic decay rate. The effects of FST-induced boundary-layer transition studied by Ovchinnikov [25], indicate that the onset of transition is dependent on the FST length scale. In the absence of data pertaining to the FST-length scale from the experiments, the length at the inlet had to be raised to a suitable value, in an attempt to match the experimental stream-wise decay rate established by Roach and Brierley [28]. Table 4.6 depicts the turbulence specifications of the simulations.

WALLS: No slip boundary is specified at the walls. For pressure, a zero Neumann condition is prescribed at the wall, inlet and outlet.

OUTFLOW BOUNDARY: At the outflow boundary, a convective boundary condition is used for describing the velocity. Due to the increase in the momentum thickness layer growth along the stream-wise direction and the symmetry boundary condition on face(3-2-6-7). It is defined as:

$$\frac{\partial \phi}{\partial t} + U_o \frac{\partial \phi}{\partial x_i} = 0 \qquad (4.1)$$

where, U_o is the free-stream velocity.

4.2.3 Numerical method

The simulations are carried out using an in-house incompressible, finite-volume based code, namely CALC-LES. For space discretization, the central-differencing scheme is used for all the velocity equations. The Crank-Nicolson method is used for time dicretization of all the equations. The numerical procedure as explained by Davidson and Peng [11], is based on an implicit, fractional step technique with a multigrid pressure poisson solver and a non-staggered grid system.

5

Results and Discussion

5.1 Post processing of results

The simulations are initially run for 3 through-flow passes $(L_x/U_o) \simeq 30$ms, before the sampling is started in order to ensure statistical steady state is achieved. The sampling is carried out for a time equivalent to 10 through-flow passes (L_x/U_o) $\simeq 400$ms. The CFL (Courant number) during the simulation was reported as $\simeq 0.3$. The onset of transition is based on the dimensionless coefficient i.e the skin friction coefficient C_f. C_f is computed as:

$$C_f = 2\frac{\tau_w}{U_o^2} \tag{5.1}$$

where, τ_w is the local wall shear stress and U_o is the free-stream velocity.

The second dimensionless coefficient used to verify laminar-turbulent transition is the Shape factor: $H= \delta^*/\theta$, where, δ^* is the displacement thickness and θ is the momentum thickness.

$$\delta^* = \int_0^\infty (1 - \frac{u(y)}{U_o})dy \tag{5.2}$$

$$\theta = \int_0^\infty \frac{u(y)}{U_o}(1 - \frac{u(y)}{U_o})dy \tag{5.3}$$

where, U_o is velocity in the free-stream outside the boundary layer, and y is the coordinate normal to the wall.

5.2 Comparison with experimental results

In this section, the results from the experimental study [28] are compared with those from the simulations. As mentioned earlier, the simulations are carried out using three different SGS modelling techniques, Smagorinsky, WALE and Scale-similarity. Additional comparisons with the experimental data can be found in the Appendix.

5.2.1 Skin friction

Figure 5.1 depicts the comparison of skin friction coefficient C_f with respect to the stream-wise Reynolds number(Re_x) over the flat plate. The calculated skin

friction coefficient, C_f and stream-wise Reynolds number(Re_x) are scaled logarithmically. It can be seen that the three models (Smagorinsky, WALE and Scale-similarity) appear to be in good agreement at the upstream of the computational domain(approximately up to the region with Reynolds number $\simeq 25000$) with the experimental data qualitatively. The location of transition onset agreed with the experiments adequately but further downstream the change in the skin friction coefficient (the region from Reynolds number $\simeq 25000$ up to Reynolds number $\simeq 65000$), appears to be damped in comparison to experimental data [28]. The Smargorinsky model estimates the skin friction coefficient in the transition region slightly better than the WALE and the Scale-similarity models respectively. The WALE and the Scale-similarity models predict the skin friction coefficient in a similar manner. The calculated skin friction coefficient is in agreement with the experimental data [28] in the region post transition(region downstream with Reynolds number $\simeq 65000$).
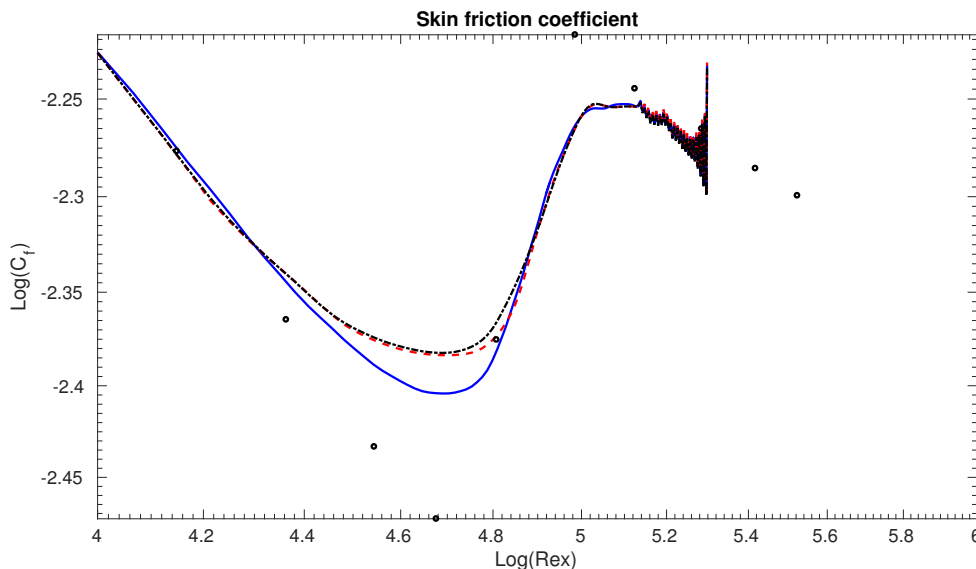
Figure 5.1: Skin friction coefficient; Legend: ∘ Experimental; − Smargorinsky; −− WALE; − · − Scale-similarity

The simulations show a lower deceleration of flow near the wall as compared to the experiments. The overall shape of the skin friction coefficient profile in the simulations suggests that the local flow over the flat plate does not adequately undergo transition from laminar to turbulent flow.

5.2.2 Shape factor

Figure 5.2 depicts the comparison of shape factor, H with respect to the stream-wise Reynolds number (Re_x) over the flat plate. The stream-wise Reynolds number (Re_x) is scaled logarithmically. It can be seen that the three models (Smagorinsky, WALE and Scale-similarity) appear to be in good agreement with the experimental data qualitatively. The location of transition onset agreed with the experiments adequately but further downstream the change in the shape factor(the region from Reynolds number $\simeq 25000$ up to Reynolds number $\simeq 65000$), appears to be damped

in comparison to experimental data [28]. The Smargorinsky model estimates the shape factor in the transition region better than the WALE and the Scale-similarity models respectively. The WALE and the Scale-similarity models predict the shape factor in a similar manner. The calculated shape factor is in agreement with the experimental data [28] in the region post transition (region downstream with Reynolds number $\simeq 65000$).
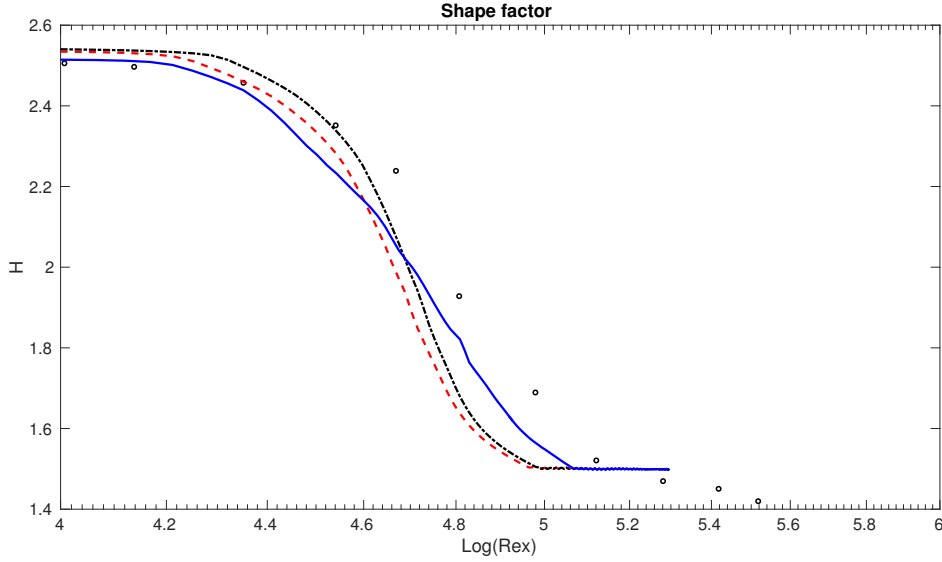
Figure 5.2: Shape factor; Legend: ∘ Experimental; — Smargorinsky; −− WALE; − · − Scale-similarity

The overall shape of the shape factor profile in the simulations suggests that the local flow over the flat plate undergoes laminar to turbulent transition.

5.3   Mesh independence study

As mentioned in Chapter 4, two sets of meshes are studied (see Table 4.2). MESH-II has a better stream-wise resolution than MESH-I, and has twice the number of sample nodes than MESH-I. Figures 5.3 & 5.4 depicts the C_f and H profiles over the flat plate for the MESH-II. It can be seen that the skin friction coefficient and shape factor profile overlaps completely in both the cases. It implies that the stream-wise resolution of the domain has no significant effect on the transition. The C_f profiles follow the experimental curve very closely for a very short distance the transition zone. It shows an initial drop for a while, but then increases in the middle of the transition zone. The increase indicates that the non-linear interactions in the boundary layer have been triggered, but it fails to grow in accordance with the experimental data.

Skin friction coefficient
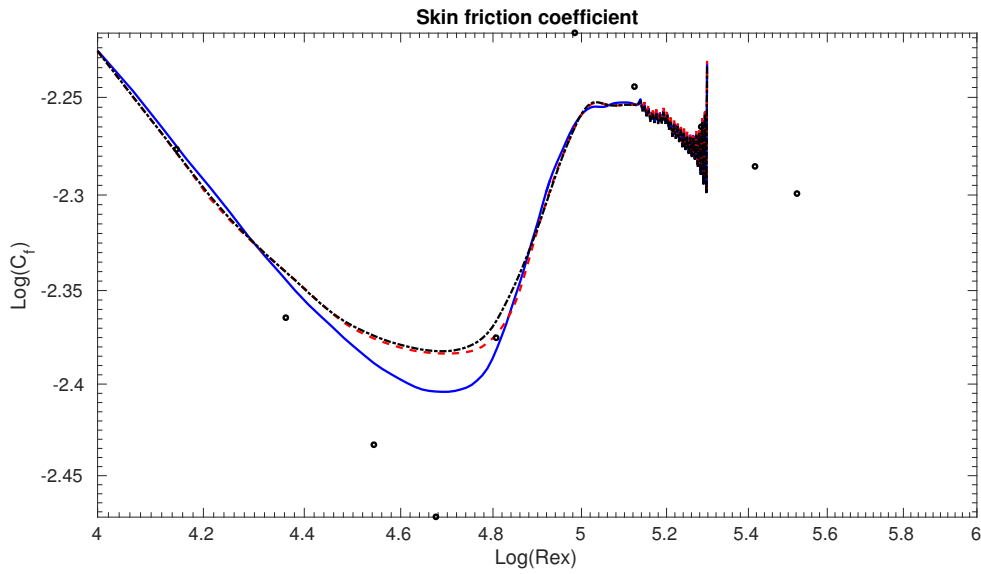
Figure 5.3: Skin friction coefficient; Legend: ∘ Experimental; − Smargorinsky; −− WALE; − · − Scale-similarity
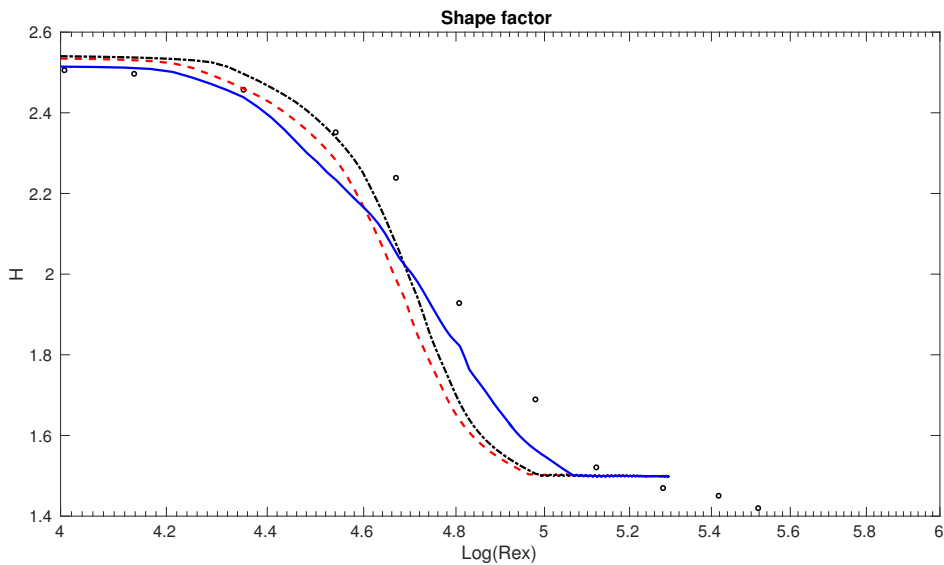
Shape factor

Figure 5.4: Shape factor; Legend: ∘ Experimental; − Smargorinsky; −− WALE; − · − Scale-similarity

5.4 Boundary layer study

In the following section, the flow in the boundary layer is discussed, in order to understand why the simulations do not comply with experimental data. In addition, the results from the Smagorinsky, WALE and Scale-similarity models are presented. All the results in this section pertain to the simulations carried out on MESH-I. The Resolved Reynolds stresses are plotted at four stream-wise stations ($25,45,95,195mm$ from the leading edge of the flat plate).
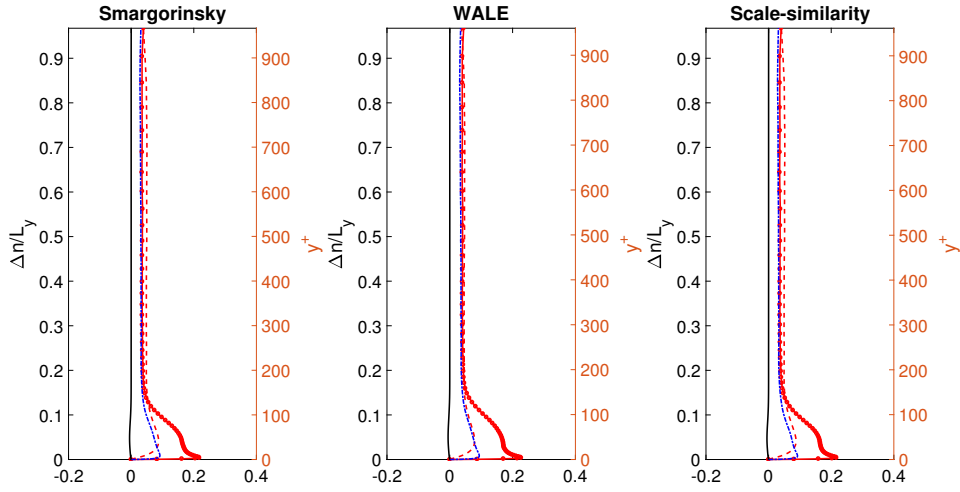
Figure 5.5: Stresses at $x = 25mm$; Legend: $- \circ - \langle u'_s u'_s \rangle$; $-- \langle u'_n u'_n \rangle$; $- \cdot - \langle u'_z u'_z \rangle$; $- \langle u'_s u'_n \rangle$
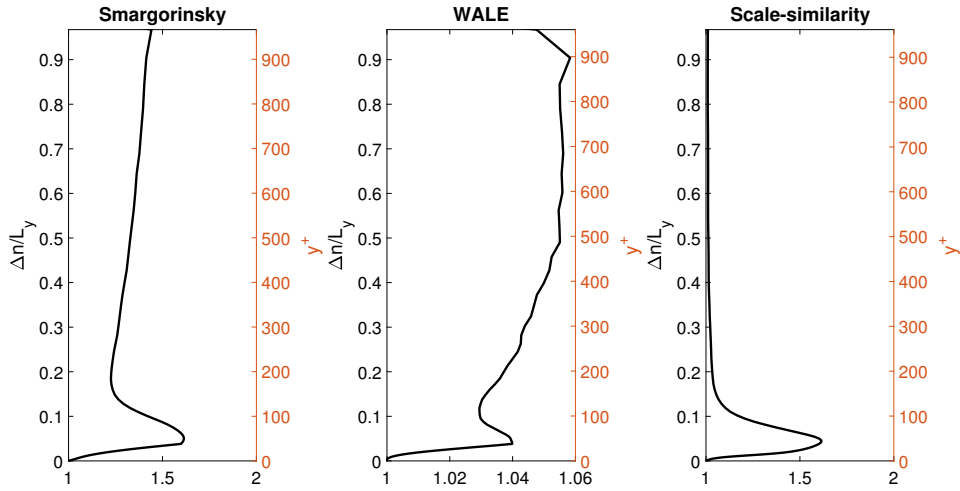
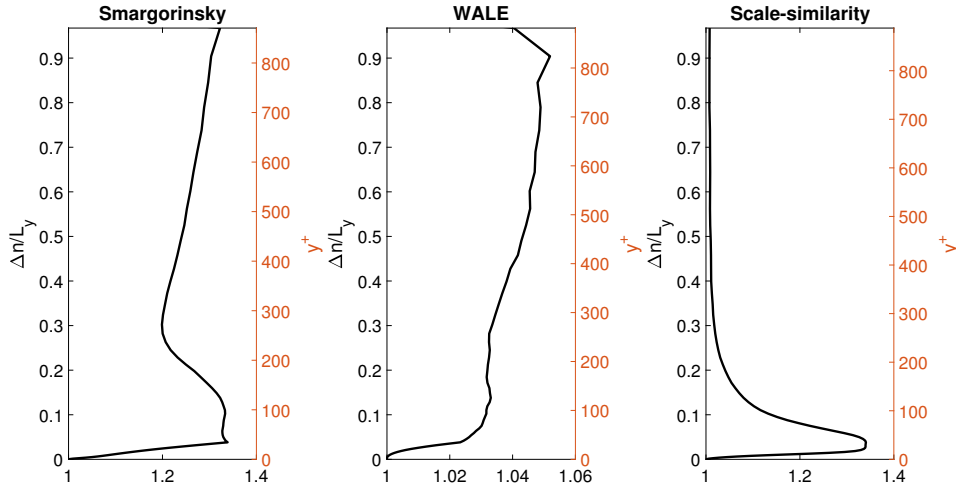**Figure 5.6:** Total viscosity at at $x = 25mm$; Legend: $- \nu_{tot}/\nu$

The Resolved Reynolds stresses are normalized with the free-stream velocity U_o. All the variables plotted at these stations over the flat plate are with respect to the wall with one axis parallel to the wall in the stream-wise direction (subscript "s") and the other normal to the wall pointing into the domain (subscript "n"). The third axis (subscript "z") is parallel to the span-wise direction in the global coordinate system. The stresses and fluxes will be plotted with respect to the normal distance from wall (Δn) scaled by the length of the domain in the wall normal direction (L_y). A second axis is also shown depicting the y^+ values corresponding the normal distance. Also, plotted are the maximum resolved turbulent kinetic energy (TKE), k_t over the flat plate.
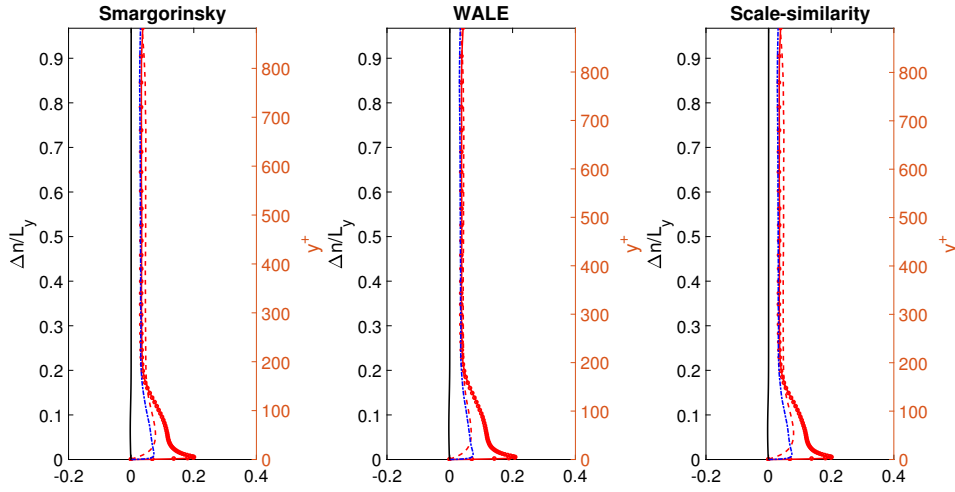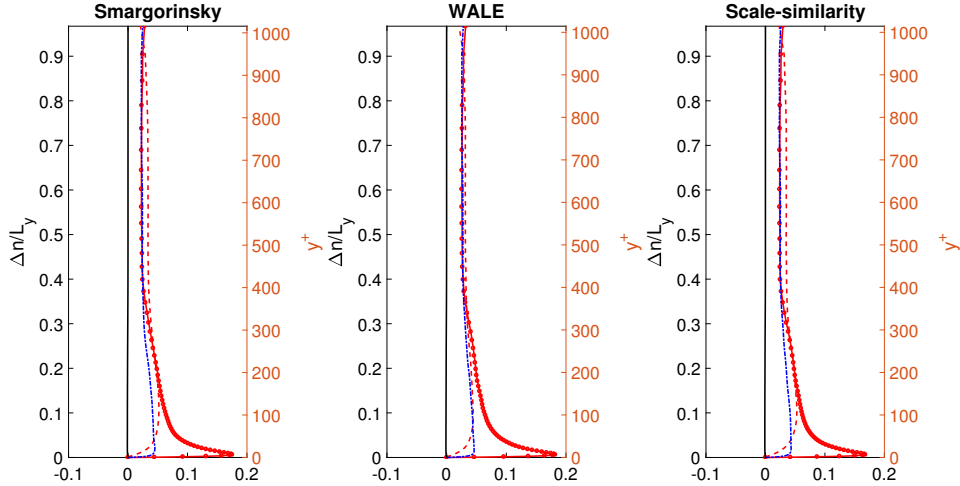
Figure 5.7: Stresses at $x = 45mm$; Legend: $- \circ - \langle u'_s u'_s \rangle$; $-- \langle u'_n u'_n \rangle$; $- \cdot - \langle u'_z u'_z \rangle$; $- \langle u'_s u'_n \rangle$
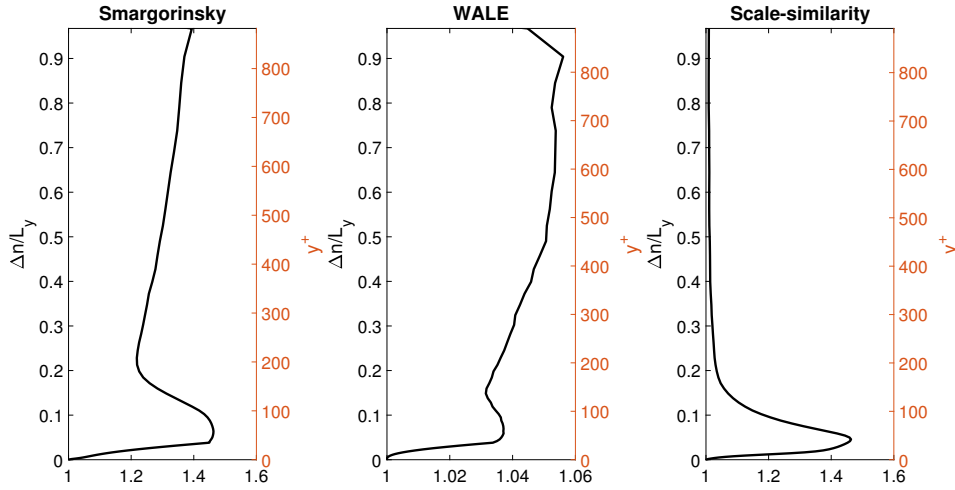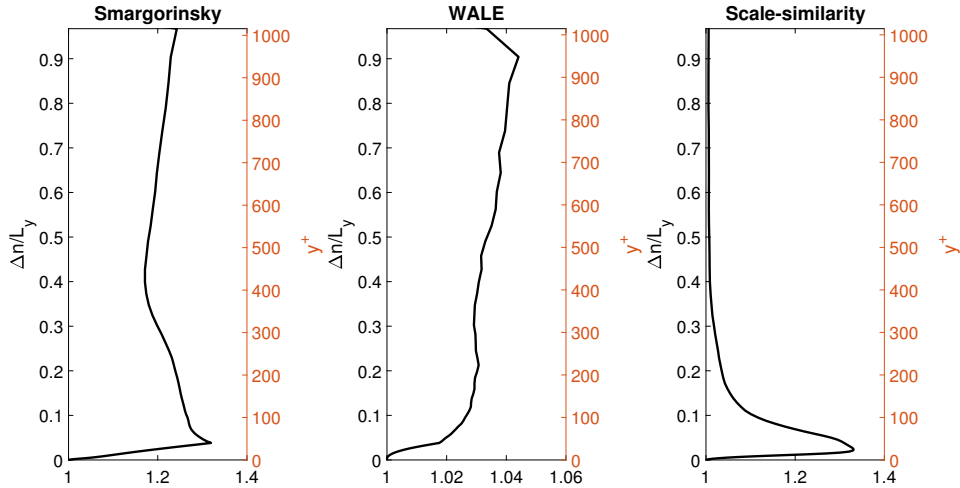

Figure 5.8: Total viscosity at at $x = 45mm$; Legend: $- \nu_{tot}/\nu$

5.4.1   Resolved stresses

Figure 5.5 illustrates the stress values at the first station (at $25mm$ from the leading edge). Figure 5.6 depicts the total viscosity ($\nu_{tot} = \nu + \nu_r$) scaled by kinematic viscosity (ν) at the point corresponding to those in the Figure 5.6. It can be seen in Figure 5.5 that with the three models, stress in the stream-wise direction, $\langle u'_s u'_s \rangle$ is the largest. In can be noted that the wall normal component $\langle u'_n u'_n \rangle$ as well as the span-wise component $\langle u'_z u'_z \rangle$ of the stress are considerably lower to the stream-wise component $\langle u'_s u'_s \rangle$ very close to the wall. The stresses seem to be more damped than in the WALE case, whereas the stresses predicted almost similarly by the Smargorinsky and Scale-similarity models respectively. In the scale-similarity case, the positive values of ν_r can be seen near the walls ($\nu_{tot}/\nu > 1$), indicating the absence of backscatter.

Figure 5.7 and Figure 5.8 represent the stresses and the total viscosity at the second station (at $45mm$ from the leading edge). This station lies approximately in the locally accelerating part of the domain(approximately at $Re_x \simeq 25000$). It can be seen that the stream-wise component of stress, $\langle u'_s u'_s \rangle$ is the most dominating part in comparison to the other components. This region of the boundary layer is probably indicates that the flow is beginning to get turbulent.
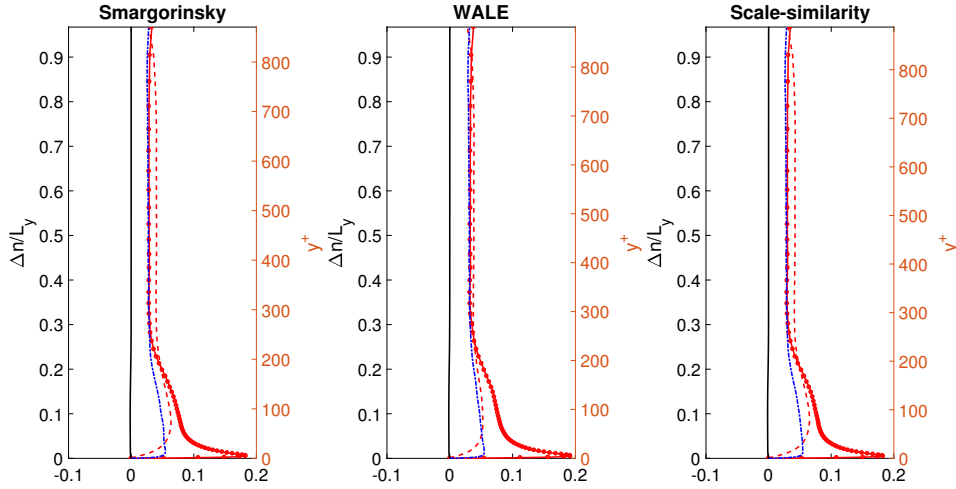
Figure 5.9: Stresses at $x = 95mm$; Legend: $- \circ - \langle u'_s u'_s \rangle$; $-- \langle u'_n u'_n \rangle$; $- \cdot - \langle u'_z u'_z \rangle$; $- \langle u'_s u'_n \rangle$

Figure 5.10: Total viscosity at at $x = 95mm$; Legend: $- \nu_{tot}/\nu$

Figure 5.9 and Figure 5.10 illustrate the stresses and total viscosity at the third station (at $95mm$ from the leading edge). It can be seen that $\langle u'_s u'_s \rangle$ is still very large as compared to the other components. Also, it can be seen the boundary layer thickness has increased considerably, as this stream-wise component is much bigger than the corresponding value at the second section even farther away from the wall.

In addition, the low y^+ values show that the wall friction velocity has decreased with respect to the upstream, as the local flow is decelerating. According to the experiments (section 5.2), at this station, the boundary layer is on the verge of attaining full turbulence, implying that the other components, namely wall-normal (n-direction) and span-wise (z-direction), should have increased significantly. It can be inferred that in the present simulations, the non-linear interactions are responsible for transition as the distribution of stresses in directions are considerably lower.

Figure 5.11: Stresses at $x = 195mm$; Legend: $-\circ-$ $\langle u'_s u'_s \rangle$; $--$ $\langle u'_n u'_n \rangle$; $-\cdot-$ $\langle u'_z u'_z \rangle$; $-$ $\langle u'_s u'_n \rangle$

Figure 5.12: Total viscosity at at $x = 195mm$; Legend: $-$ ν_{tot}/ν

Figure 5.11 and Figure 5.12 represent the stresses and total viscosity at the fourth station (at $195mm$ from the leading edge). At this station, as per the experiments, the boundary layer should have gone completely turbulent. This is characterized by means of an isotropic distribution of stresses in all directions except for the wall-normal component close to the wall. This is not found in the present simulations.

The span-wise component $\langle u'_z u'_z \rangle$ shows a slight decrease close to the wall and the wall-normal component $\langle u'_n u'_n \rangle$ slightly away from the wall, both compared to their corresponding values at the upstream stations (Figure 5.5 and Figure 5.7). There are signs of growing turbulence, as emphasized by the shape factor plot in figure 5.2. At this station, the boundary layer thickness has increased considerably and the normal components of stress $\langle u'_n u'_n \rangle$ and $\langle u'_z u'_z \rangle$ are significant compared to the upstream stations.

In conclusion to the analysis of Reynolds stresses in the boundary layer, it can be said that there is a definite decrease in the stream-wise stress component as the flow moves downstream, while the same cannot be said for the wall-normal and span-wise components. The Smagorinsky, WALE and Scale-similarity models predict similar behaviour and the difference is not significant. As a result, the numerical oscillations created this way help in sustaining turbulence and do not dampen out. In addition, if they can act as sources of disturbance, as provided by FST, and whether they invoke the non-linear modes is not known. The numerical fluctuations do not mimic the FST as provided in the experiments, hence it fails to trigger transition appropriately. The peaks seen in the intensities at the downstream of the flow i.e region with Reynolds number > 65000, broadly at the correct position and with the correct magnitude, .indicate that the LES captures the essential fluid dynamics occurring in the turbulent layer, but it does not give considerable confidence that the true physical processes of bypass transition are being reproduced numerically. The profiles of the principal Reynolds stress $\langle u'_s u'_n \rangle$ at $x = 45mm$ and $x = 95mm$. The predictions are clearly high relative to the experimental data as shown in the Appendix). It is not known what aspect of the current LES simulations are at fault but in the light of the general level of agreement obtained, we conclude that,the the simulation qualitatively mimics ,the real boundary layer, even though precise quantitative, agreement is not found for all variables.

5.4.2   Turbulent kinetic energy and *rms* fields

In this section the maximum of turbulent kinetic energy (TKE) and *rms* fields over the flat plate is studied. Along with the TKE (k_t), the stream-wise ($\langle u'_s u'_s \rangle$), wall normal velocity field ($\langle u'_n u'_n \rangle$) and span-wise ($\langle u'_z u'_z \rangle$) velocity fields are studied. The aim is to study the evolution of the fluctuating fields over the wall. In bypass transition, these fluctuations grow appreciably while going from laminar to turbulent phase. Plots from the Smagorinsky, WALE and Scale-similarity models are demonstrated.

Figure 5.13, depicts the maximum of TKE $(k_t)|_{max}$ over the plate surface. It also depicts the maximum values of the stream-wise $\langle u'_s u'_s \rangle |_{max}$, wall normal $\langle u'_n u'_n \rangle |_{max}$ and span-wise $\langle u'_z u'_z \rangle |_{max}$ fluctuating velocity components. The TKE $(k_t)|_{max}$ and other fluctuating fields are normalized with respect to the free-stream velocity U_o. As per the experiments, the transition zone lies between $x=45mm$ ($Re_x=25000$) and $x=95mm$ ($Re_x=65000$), as per Figure 5.1. Over the plate surface, the Smargorinsky, WALE and Scale-similarity models there is a sudden jump in TKE corresponding
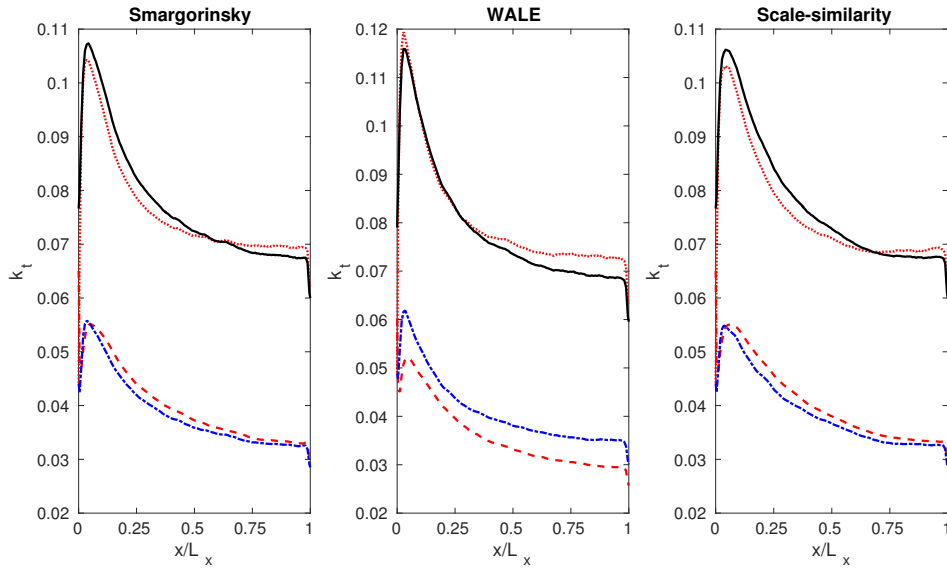
Figure 5.13: Peak TKE k_t over the surface; Legend: $-\ k_t|_{max}$; $\cdots \langle u_s' u_s' \rangle|_{max}$; $--\ \langle u_n' u_n' \rangle|_{max}$; $-\cdot-\ \langle u_z' u_z' \rangle|_{max}$

to the experimentally measured trigger point, but then it decays steadily further downstream. It can be concluded that the fluctuations grow in amplitude inside the boundary layer and can be associated to the appearance of stream-wise streaks in the boundary layer. Bypass transition is associated with the free-stream turbulence interacting with the boundary layer in order to force transition. In the present case, the streaks are formed but unable to sustain due to the absence of forcing by FST as the maximum fluctuation level remains almost constant at the downstream.

Figure 5.13, depicts the maximum of normal fluctuations $\langle u_n' u_n' \rangle \mid_{max}$ over the plate surface. It can be observed that the predicted peak fluctuations normal fluctuations $\langle u_n' u_n' \rangle \mid_{max}$ and $\langle u_z' u_z' \rangle \mid_{max}$ are negligible in comparison to the stream-wise fluctuations $\langle u_s' u_s' \rangle \mid_{max}$. The lack of such fluctuations in the boundary layer shows that there is no real transition in the boundary layer.

6

Conclusions and Future Work

6.1 Conculsions

It can be concluded from simulations conducted in the present study that the transition observed cannot justify the experimental findings. The skin friction coefficient(C_f) as well as the shape factor H profile from the simulations do not show complete agreement with the experimental data, although they do suggest the occurrence of laminar-turbulent transition. The non-linear mechanisms inside the boundary layer responsible for transition appear to not get triggered sufficiently by the artificial fluctuations used as FST in the simulations.

The boundary layer study showed a gradual decrease in the stream-wise fluctuations along the plate surface, as evident from the decrease in the stream-wise component of resolved stress. However, the other components, namely, the span-wise and wall-normal components of resolved normal stress, do not show any significant increment. The reason for the absence of energy distribution, over the plate surface is not clear. Probably, the growth in stream-wise fluctuations is not enough to force production in the other directions.

The study of the peak TKE (k_t) showed that the fluctuations grow appreciably near the experimentally observed transition point. It also indicates a growth of stream-wise streaks in comparison to the wall normal and span-wise fluctuations. Also as discussed in the literature survey, the wall normal component of the fluctuations plays an important role in triggering transition, thereby proving the absence of non-linear interactions triggering transition. It can be attributed to the necessity of continuous forcing provided by the FST for these fluctuations to be maintained. More about it can be understood by the nature of FST turbulence outside the boundary layer in this region.

A mesh with a finer resolution in the stream-wise direction did not show any significant effect on the transition. The C_f and H profile followed the experimental data only in the upstream (laminar) as well as the downstream (turbulent) of the transition point but did not agree well experimentally defined transition point. One of the possibilities concluded is that there is a need for a very fine stream-wise resolution throughout the surface to enable the continuous interaction of non-linear modes.

6.2   Future Work

According to the literature survey the effect of considering the leading edge as well as the concept of shear sheltering is explained briefly. It would be interesting to analyze how the turbulence evolves from the inflow boundary till it reaches the leading edge, and how the low frequency modes be allowed to enter the boundary layer with the leading edge effects. Also, it would be interesting to observe the results for simulations conducted on the entire flat plate rather than a limited computational domain and see whether it makes any significant changes to the results. The results are also dependent on the choice of discretization schemes and other SGS models and the effect on these parameters can also be studied.

A

Mesh resolution in wall units
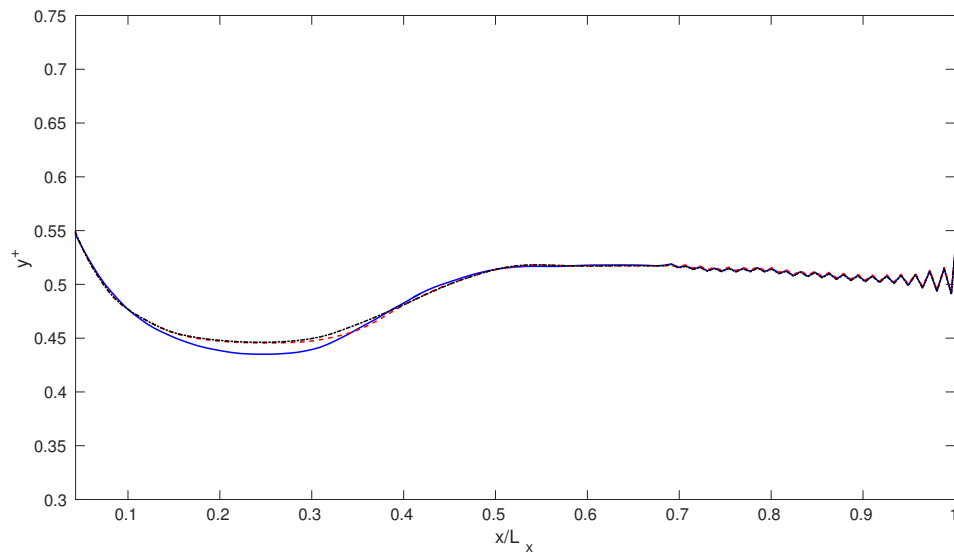
Figure A.1: Wall y^+ units; Legend: — Smargorinsky; −− WALE; − · − Scale-similarity. X-coordinates are scaled by the stream-wise length L_x.

B
Comparison of mean velocity with experimental data
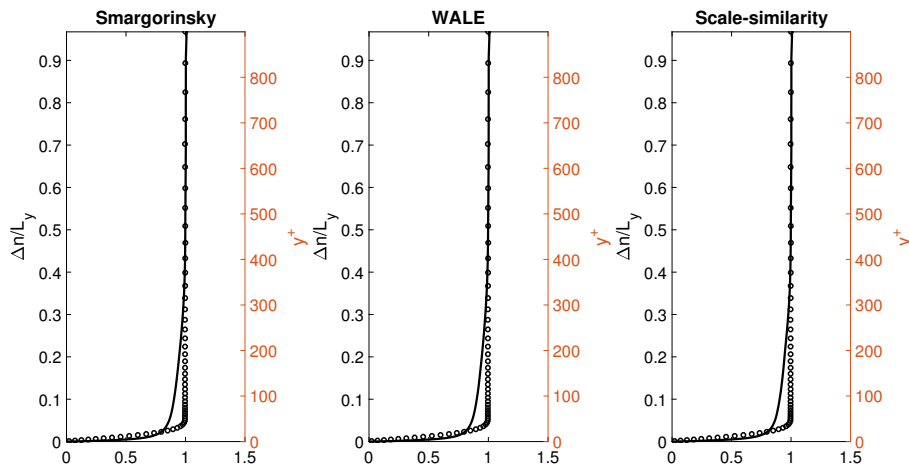
Figure B.1: Mean velocity U at $x = 25mm$; Legend: $-$ LES; $\circ$ Experimental; Mean velocity scaled with the free-stream velocity U_o
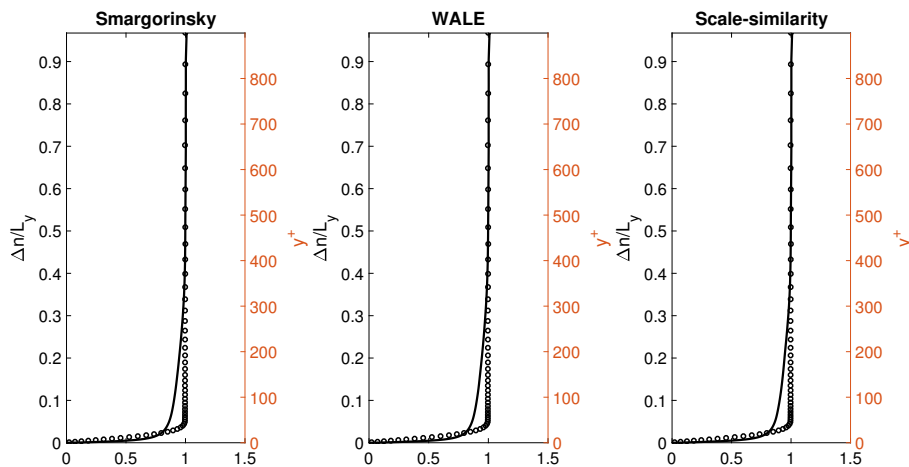

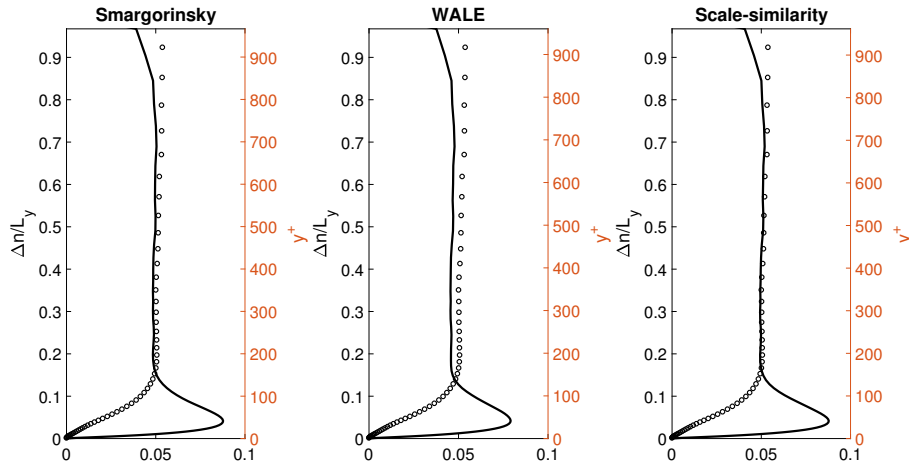**Figure B.2:** Mean velocity U at $x = 45mm$; $-$ LES; $\circ$ Experimental; Mean velocity scaled with the free-stream velocity U_o
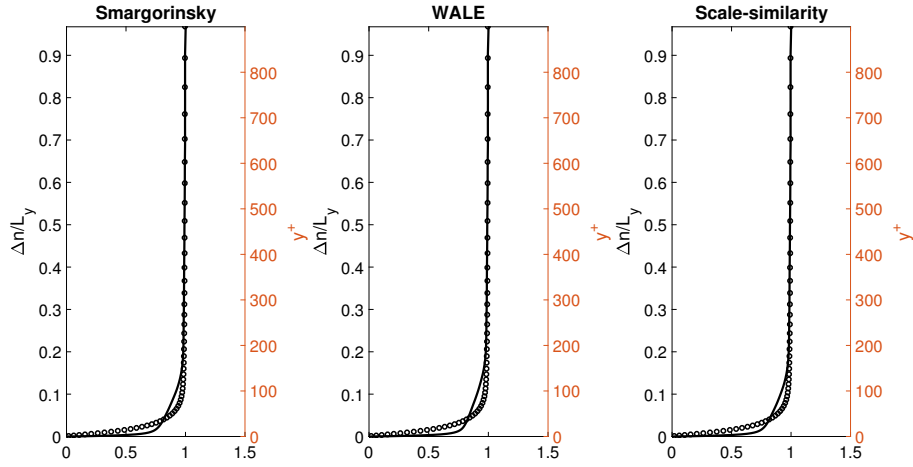
Figure B.3: Mean velocity U at $x = 95mm$; $-$ LES; $\circ$ Experimental; Mean velocity scaled with the free-stream velocity U_o
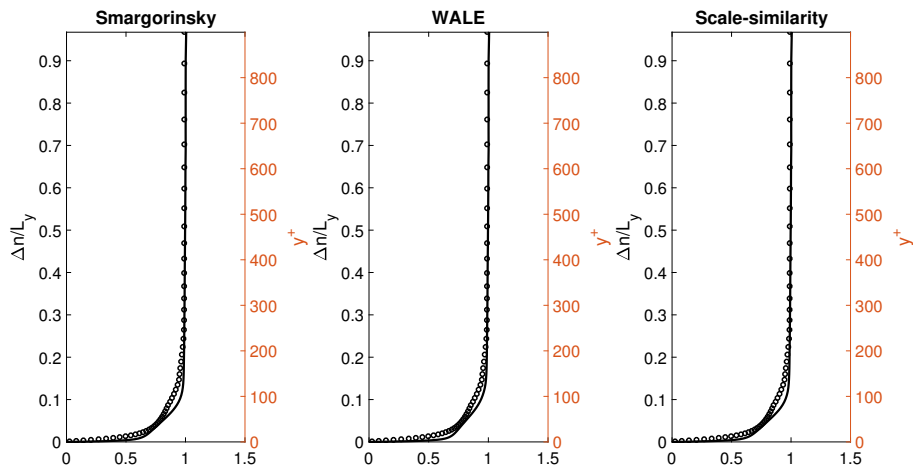
Figure B.4: Mean velocity U at $x = 195mm$; $-$ LES; $\circ$ Experimental; Mean velocity scaled with the free-stream velocity U_o

C

Comparison of u_{rms} with experimental data
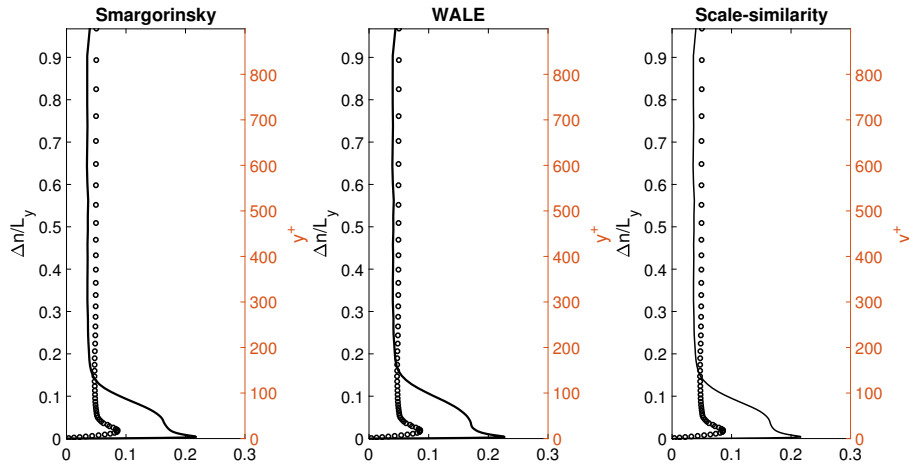
Figure C.1: Velocity fluctuation u_{rms} at $x = 25mm$; Legend: $-$ LES; $\circ$ Experimental; rms velocity scaled with the free-stream velocity U_o
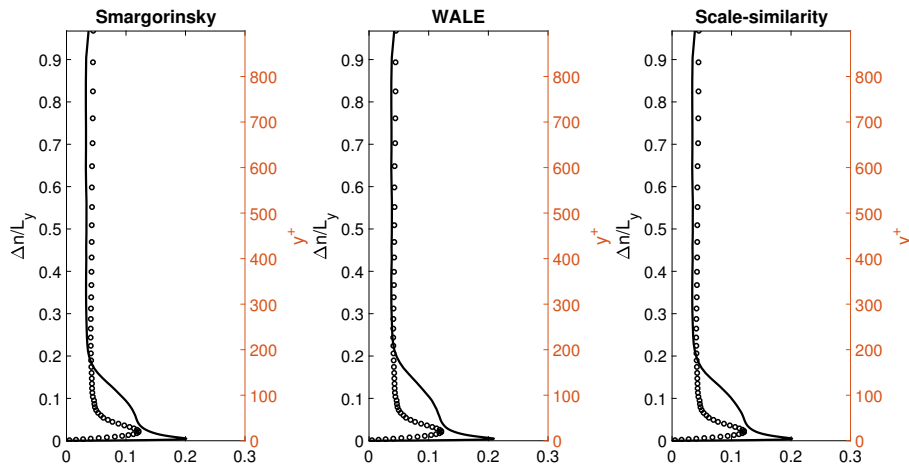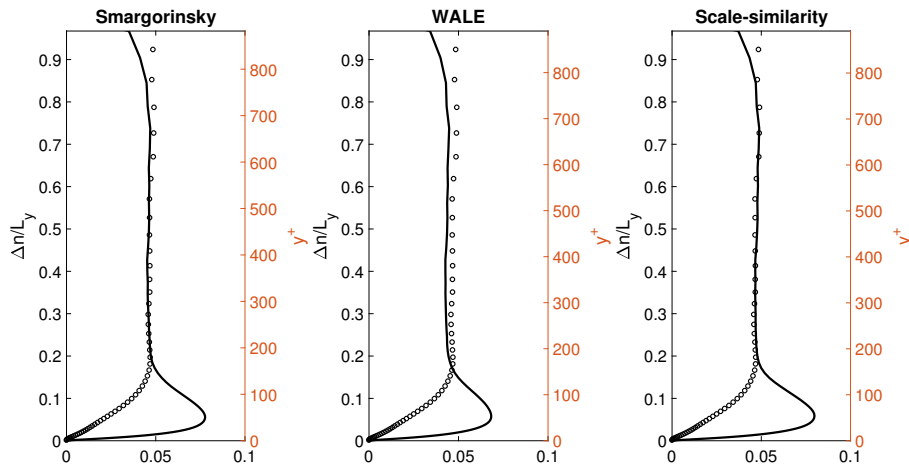

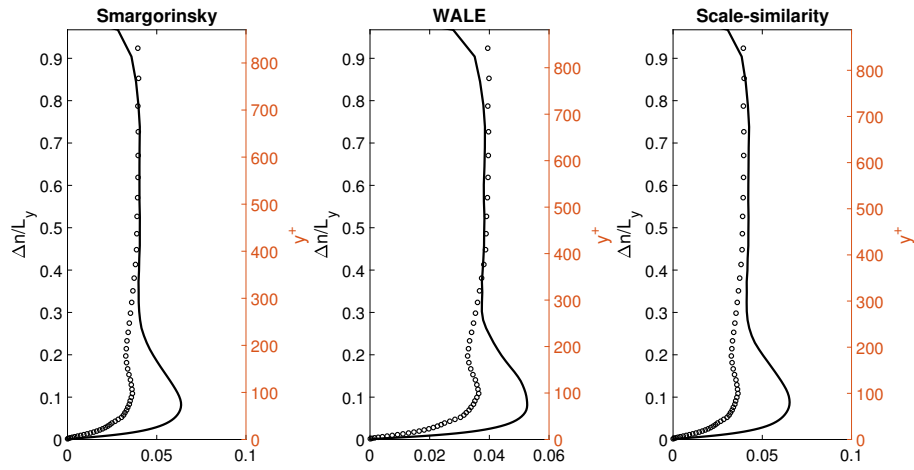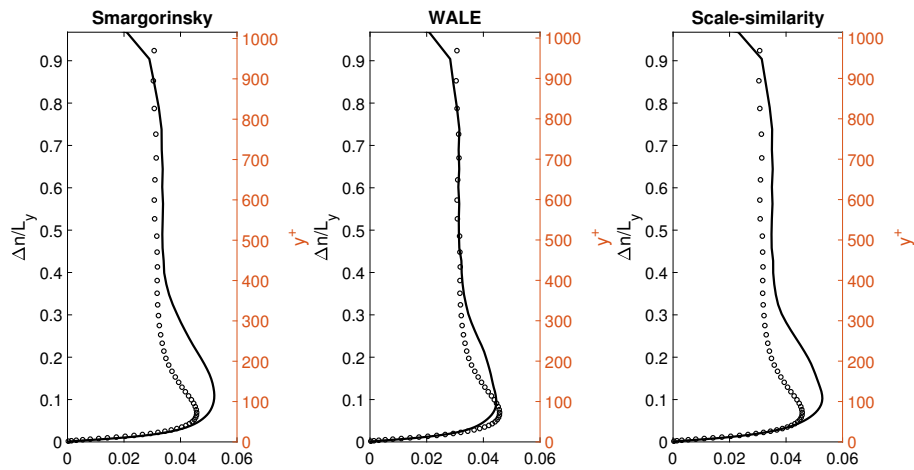**Figure C.2:** Velocity fluctuation u_{rms} at $x = 45mm$; Legend: $-$ LES; $\circ$ Experimental; rms velocity scaled with the free-stream velocity U_o
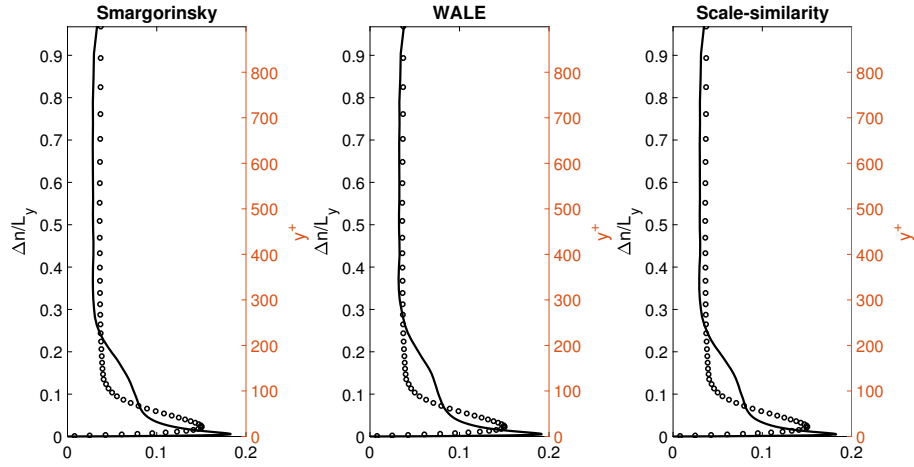
Figure C.3: Velocity fluctuation u_{rms} at $x = 95mm$; Legend: $-$ LES; $\circ$ Experimental; *rms* velocity scaled with the free-stream velocity U_o
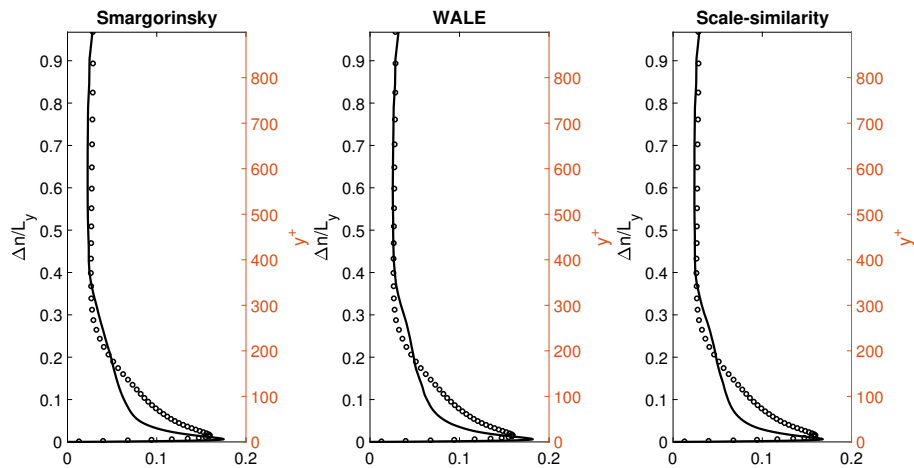
Figure C.4: Velocity fluctuation u_{rms} at $x = 195mm$; Legend: $-$ LES; $\circ$ Experimental; *rms* velocity scaled with the free-stream velocity U_o

D

Comparison of v_{rms} with experimental data

Figure D.1: Velocity fluctuation v_{rms} at $x = 25mm$; Legend: $-$ LES; $\circ$ Experimental; rms velocity scaled with the free-stream velocity U_o

Figure D.2: Velocity fluctuation v_{rms} at $x = 45mm$; Legend: $-$ LES; $\circ$ Experimental; rms velocity scaled with the free-stream velocity U_o
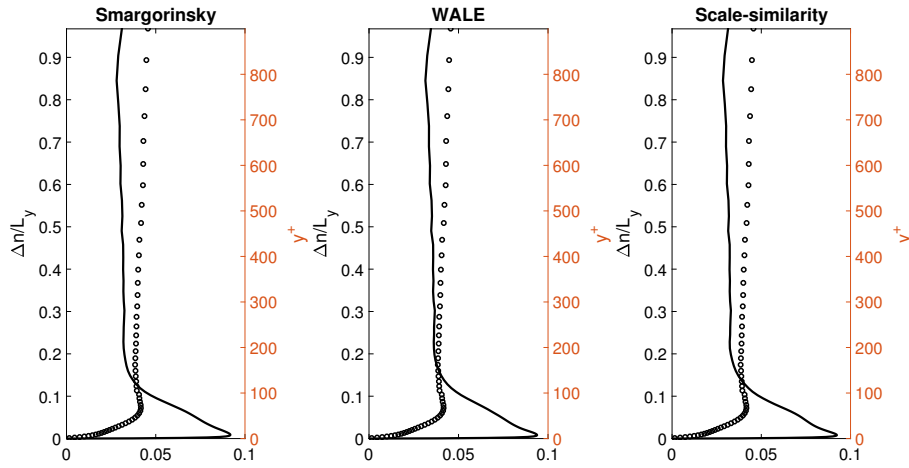
Figure D.3: Velocity fluctuation v_{rms} at $x = 95mm$; Legend: $-$ LES; $\circ$ Experimental; rms velocity scaled with the free-stream velocity U_o
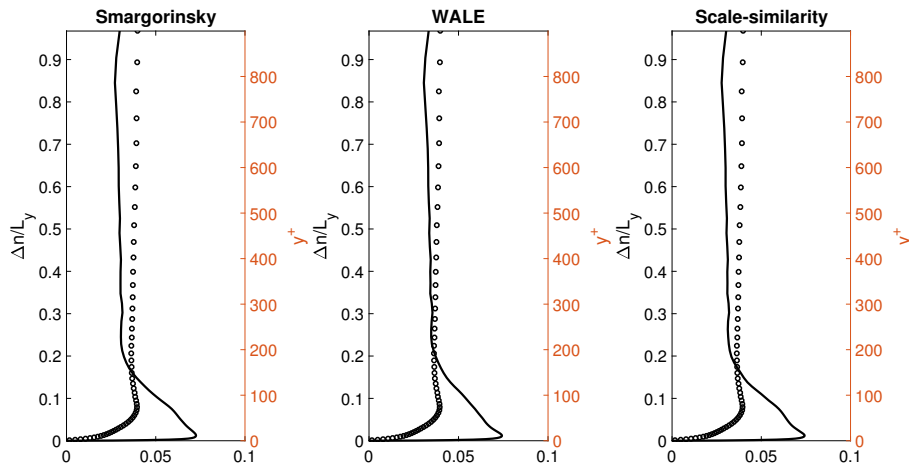

Figure D.4: Velocity fluctuation v_{rms} at $x = 195mm$; $-$ LES; $\circ$ Experimental; rms velocity scaled with the free-stream velocity U_o
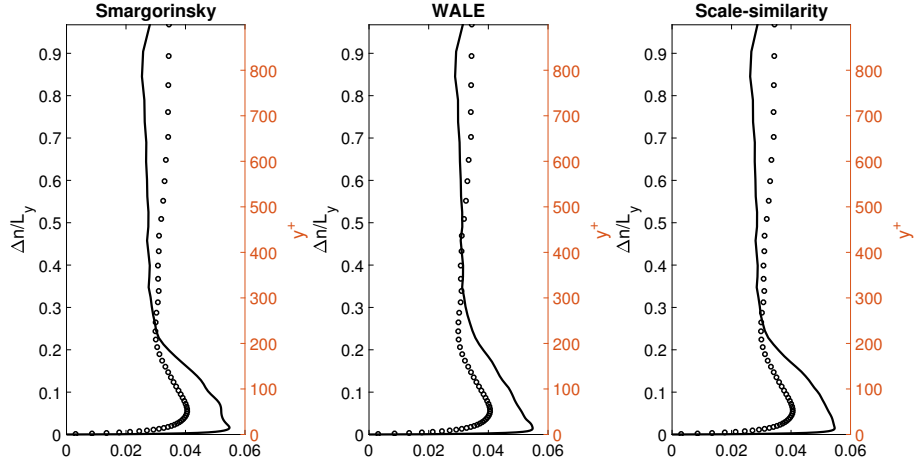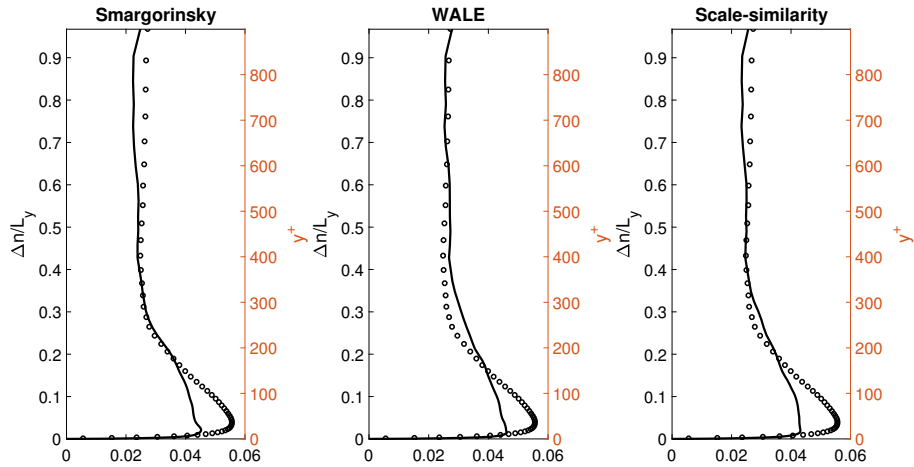
E

Comparison of w_{rms} with experimental data

Figure E.1: Velocity fluctuation w_{rms} at $x = 25mm$; $-$ LES; $\circ$ Experimental; rms velocity scaled with the free-stream velocity U_o

Figure E.2: Velocity fluctuation w_{rms} at $x = 45mm$; $-$ LES; $\circ$ Experimental; rms velocity scaled with the free-stream velocity U_o
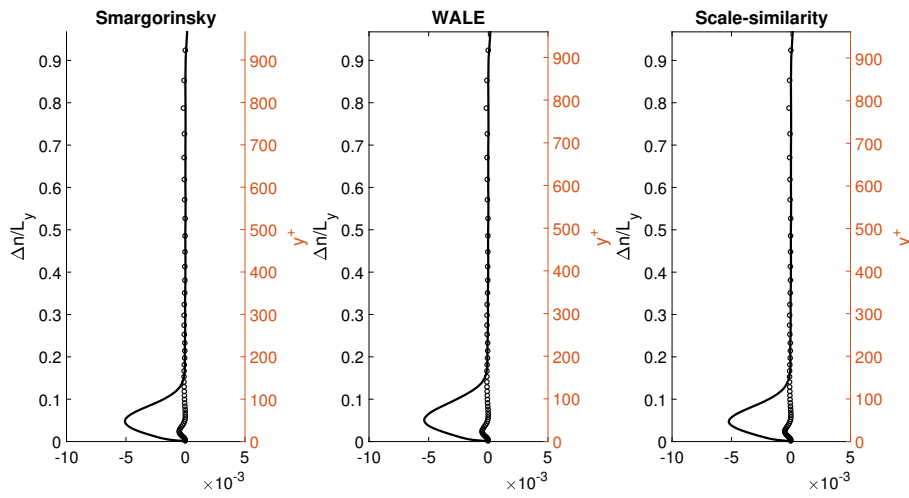
Figure E.3: Velocity fluctuation w_{rms} at $x = 95mm$; $-$ LES; $\circ$ Experimental; rms velocity scaled with the free-stream velocity U_o
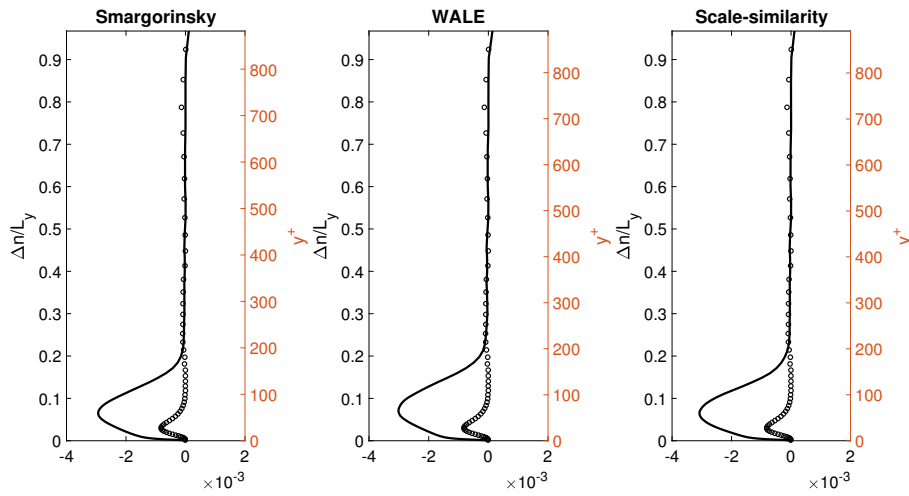

Figure E.4: Velocity fluctuation w_{rms} at $x = 195mm$; $-$ LES; $\circ$ Experimental; rms velocity scaled with the free-stream velocity U_o
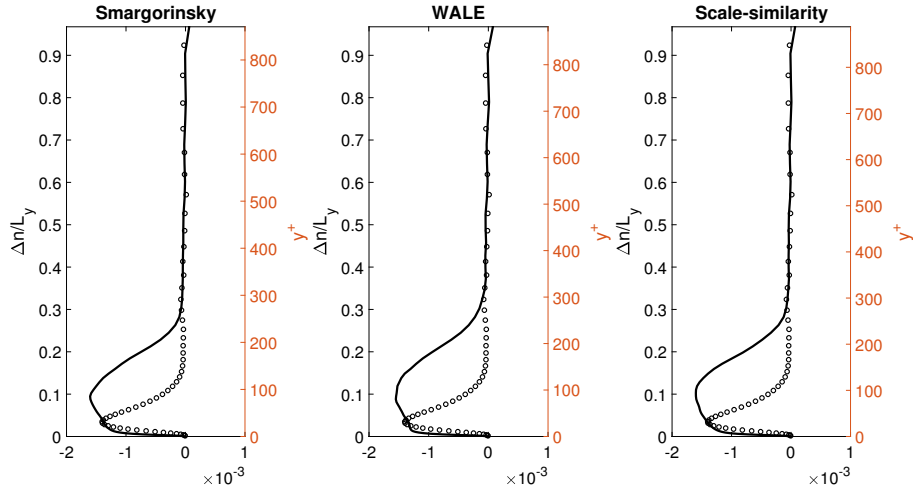
F

Comparison of $\langle u'v' \rangle$ with experimental data
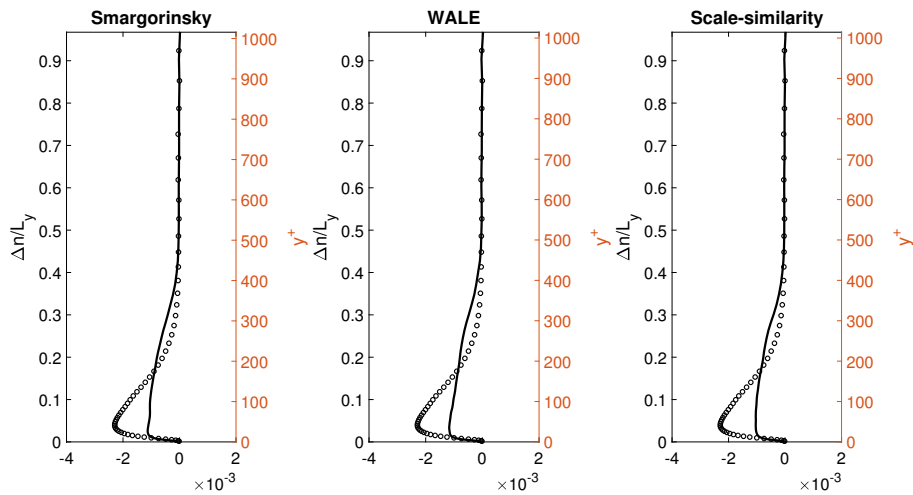

Figure F.1: Principal stress $\langle u'v' \rangle$ at $x = 25mm$; $-$ LES; $\circ$ Experimental; $\langle u'v' \rangle$ velocity scaled with the free-stream velocity U_o^2

Figure F.2: Principal stress $\langle u'v' \rangle$ at $x = 45mm$; $-$ LES; $\circ$ Experimental; $\langle u'v' \rangle$ velocity scaled with the free-stream velocity U_o^2

Figure F.3: Principal stress $\langle u'v' \rangle$ at $x = 95mm$; Legend: $-$ LES; $\circ$ Experimental; $\langle u'v' \rangle$ scaled with the free-stream velocity U_o^2

Figure F.4: Principal stress $\langle u'v' \rangle$ at $x = 195mm$; $-$ LES; $\circ$ Experimental; $\langle u'v' \rangle$ scaled with the free-stream velocity U_o^2

Bibliography

[1] P. Alfredsson and M. Matsubara. "Streaky structures in transition". In: *Transitional boundary layers in aeronautics* 46 (1996), pp. 373–386.

[2] P. Andersson, M. Berggren, and D. S. Henningson. "Optimal disturbances and bypass transition in boundary layers". In: *Physics of Fluids* 11.1 (1999), pp. 134–150.

[3] J. Bardina, J. Ferziger, and W. Reynolds. "Improved subgrid scale models for large eddy simulation." In: *AIAA 80-1357* (1980).

[4] S. Berlin and D. D. Henningson. "A nonlinear mechanism for receptivity of free-stream disturbances". In: *Physics of Fluids* 11.12 (1999), pp. 3749–3760.

[5] L. Brandt, P. Schlatter, and D. S. Henningson. "Transition in boundary layers subject to free-stream turbulence". In: *Journal of Fluid Mechanics* 517 (2004), pp. 167–198.

[6] K. M. Butler and B. F. Farrell. "Three-dimensional optimal perturbations in viscous shear flow". In: *Physics of Fluids A: Fluid Dynamics* 8.4 (1992), pp. 1637–1650.

[7] S. Cherubini, P. De Palma, and J. C. Robinet. "Numerical study of the effect of freestream turbulence on by-pass transition in a boundary layer". In: *Energy Procedia* 45 (2014), pp. 578–587.

[8] S. Cherubini et al. "A purely nonlinear route to transition approaching the edge of chaos in a boundary layer". In: *Fluid Dynamics Research* 44.3 (2012).

[9] L. Davidson. "Hybrid LES-RANS: back scatter from a scale-similarity model used as forcing." In: *Philosophical transactions of The Royal Society. Series A, Mathematical, physical, and engineering sciences* 367.1899 (2009), pp. 2905–2915.

[10] L. Davidson. "Using isotropic synthetic fluctuations as inlet boundary conditions for unsteady simulations." In: *Advances and Applications in Fluid Mechanics* 1.1 (2007), pp. 1–35.

[11] L. Davidson and S. H. Peng. "Hybrid LES-RANS modelling: a one-equation SGS model combined with a $k-\omega$ model for predicting recirculating flows". In: *International Journal for Numerical Methods in Fluids* 43.9 (2003), pp. 1003–1018.

[12] S. Grossmann. "The onset of shear flow turbulence". In: *Reviews of modern physics* 72.2 (2000), p. 603.

[13] R. G. Jacobs and P. A. Durbin. "Shear sheltering and the continuous spectrum of the Orr–Sommerfeld equation". In: *Physics of Fluids* 10.8 (1998), pp. 2006–2011.

[14] R. G. Jacobs and P. A. Durbin. "Simulations of bypass transition". In: *Journal of Fluid Mechanics* 428 (2001), pp. 185–212.

[15] P. Jonas, O. Mazur, and V. Uruba. "On the receptivity of the bypass transition to as the length scale of the outer stream turbulence". In: *European Journal of Mechanics -B/Fluids* 19.5 (2000), pp. 707–722.

[16] Y. S. Kachanov. "Physical mechanisms of laminar-boundary-layer transition". In: *Annual Review of Fluid Mechanics* 26.1 (1994), pp. 411–482.

[17] J. Kendall. "Experimental study of disturbances produced in a pre-transitional laminar boundary layer by weak freestream turbulence". In: *AIAA, 18th Fluid Dynamics and Plasmadynamics and Lasers Conference* 1 (1985).

[18] P. Klebanof. "Effect of free-stream turbulence on a laminar boundary layer". In: *Bulletin of the American Physical Society* 16 (1971), p. 1323.

[19] P. Luchini. "Reynolds-number-independent instability of the boundary layer over a flat surface: optimal perturbations". In: *Journal of Fluid Mechanics* 404 (2000), pp. 289–309.

[20] D. W. Wundrow M. E. Goldstein. "On the environmental realizability of algebraically growing disturbances and their relation to Klebanoff modes". In: *Theoretical and computational fluid dynamics* 10.1-4 (1998), pp. 171–186.

[21] M. Matsubara and P. Alfredsson. "Disturbance growth in boundary layers subjected to free-stream turbulence". In: *Journal of Fluid Mechanics* 30 (2001), pp. 149–168.

[22] C. Meneveau and J. Katz. "Scale-invariance and turbulence models for large-eddy simulation". In: *Annual Review of Fluid Mechanics* 32 (2000), pp. 1–32.

[23] S. Nagarajan, S. Lele, and J. Ferziger. "Leading-edge effects in bypass transition". In: *Journal of Fluid Mechanics* 572 (2007), pp. 471–504.

[24] F. Nicoud and F. Ducros. "Subgrid-scale stress modelling based on the square of the velocity gradient tensor". In: *Flow, Turbulence and Combustion* 62.3 (1999), pp. 183–200.

[25] V. Ovchinnikov. "Inflow conditions for numerical simulations of bypass transition". PhD thesis. 2004.

[26] S. B. Pope. *Turbulent Flows.* First Edit. Cambridge University Press, 2000.

[27] A. Pradhan. *Large Eddy Simulation of flow around a Gas Turbine Outlet Guide Vane.* Tech. rep. Göteborg: Chalmers University of Technology, 2014, pp. 28–32.

[28] P. E. Roach and D. H. Brierley. "The influence of a turbulent free-stream on zero pressure gradient transitional boundary layer development". In: *Numerical Simulation of Unsteady Flows and Transition to Turbulence.* Ed. by O. Pironneau et al. New York: Cambridge University Press, 1992, pp. 319–347.

[29] W. S. Saric, H. L. Reed, and E. J. Kerschen. "Boundary-layer receptivity to freestream disturbances". In: *Annual Review of Fluid Mechanics* 34.1 (2002), pp. 291–319.

[30] A. M. Savill. "Evaluating turbulence model predictions of transition". In: *Applied Scientific Research* 51.1-2 (1993), pp. 555–562.

[31] A. M. Savill. "Numerical simulation of boundary layer transition in the presence of free stream turbulence". In: *Numerical Simulation of Unsteady Flows*

and Transition to Turbulence. Ed. by O. Pironneau et al. New York: Cambridge University Press, 1992, pp. 404–442.

[32] P. J. Schmid. "Nonmodal stability theory". In: *Annual Review of Fluid Mechanics* 39 (2007), pp. 129–162.

[33] J. Smagorinsky. "General circulation experiments with the primitive equations: Part I, The basic experiment". In: *Monthly Weather Review* 91 (1963), pp. 99–164.

[34] P. R. Voke and Z. Yang. "Numerical simulation of boundary layer transition in the presence of free stream turbulence". In: *Numerical Simulation of Unsteady Flows and Transition to Turbulence.* Ed. by O. Pironneau et al. New York: Cambridge University Press, 1992, pp. 398–402.

[35] P. R. Voke and Z. Yang. "Numerical study of bypass transition". In: *Physics of Fluids* 7.9 (1995), pp. 2256–2264.

[36] X. Wu and P. Moin. "Direct numerical simulation of turbulence in a nominally zero-pressure-gradient flat-plate boundary layer". In: *Journal of Fluid Mechanics* 630 (2009), pp. 5–41.

[37] T. A. Zaki and P. A. Durbin. "Continuous mode transition and the effects of pressure gradient". In: *Journal of Fluid Mechanics* 563 (2006), pp. 356–388.

[38] T. A. Zaki and P. A. Durbin. "Mode interaction and the bypass route to transition". In: *Journal of Fluid Mechanics 531* 531 (2005), pp. 85–111.